Metabolic reprogramming of synovial fibroblasts in osteoarthritis by inhibition of pathologically overexpressed pyruvate dehydrogenase kinases

Damerau, A., Kirchner, M., Pfeiffenberger, M., Ehlers, L., Do Nguyen, D.H., Mertins, P., Bartek, B., Maleitzke, T., Palmowski, Y., Hardt, S., Winkler, T., Buttgereit, F., Gaber, T.

This is the final version of the accepted manuscript. The original article has been published in final edited form in:

Metabolic Engineering
2022 JUL ; 72: 116-132
2022 MAR 13 (first published online: final publication)
doi: 10.1016/j.ymben.2022.03.006

Publisher: Elsevier

Article Type: Full-length article

Short Title: PDK3 in OA FLS

Full Title: Metabolic reprogramming of synovial fibroblasts in osteoarthritis by inhibition of pathologically overexpressed pyruvate dehydrogenase kinases

Authors: Alexandra Damerau[1,2], Marieluise Kirchner[3], Moritz Pfeiffenberger[1,2], Lisa Ehlers[1,2], Duc Ha Do Nguyen[1,2], Philipp Mertins[3], Benjamin Bartek[4], Tazio Maleitzke[4,5,6], Yannick Palmowski[4], Sebastian Hardt[4], Tobias Winkler[4,5,6,7], Frank Buttgereit[1,2] and Timo Gaber[1,2]*

Affiliations

[1] Charité – Universitätsmedizin Berlin, corporate member of Freie Universität Berlin and Humboldt-Universität zu Berlin, Department of Rheumatology and Clinical Immunology, Berlin, Germany

[2] German Rheumatism Research Centre (DRFZ) Berlin, a Leibniz Institute, Berlin, Germany

[3] Berlin Institute of Health and Max-Delbrück-Centrum for Molecular Medicine, Germany

[4] Charité – Universitätsmedizin Berlin, corporate member of Freie Universität Berlin and Humboldt-Universität zu Berlin, Center for Musculoskeletal Surgery, Berlin, Germany

[5] Berlin Institute of Health at Charité – Universitätsmedizin Berlin, BIH Biomedical Innovation Academy, BIH Charité Clinician Scientist Program, Berlin, Germany

[6] Julius Wolff Institute, Berlin Institute of Health at Charité – Universitätsmedizin Berlin, Germany

[7] Berlin Institute of Health Center for Regenerative Therapies, Berlin Institute of Health at Charité – Universitätsmedizin Berlin, Berlin, Germany

*** Correspondence**

Dr. rer. nat. Timo Gaber

Charité – Universitätsmedizin Berlin, Department of Rheumatology and Clinical Immunology

Charitéplatz 1, 10117 Berlin

Tel: +49 (0)30 450 513 125; Fax: +49 (0)30 450 513 917

timo.gaber@charite.de

Abstract

Osteoarthritis (OA) is the most common degenerative joint disease and a major cause of age-related disability worldwide, mainly due to pain, the disease's main symptom. Although OA was initially classified as a non-inflammatory joint disease, recent attention has been drawn to the importance of synovitis and fibroblast-like synoviocytes (FLS) in the pathogenesis of OA. FLS can be divided into two major populations: thymus cell antigen 1 (THY1)- FLS are currently classified as quiescent cells and assumed to destroy bone and cartilage, whereas THY1+ FLS are invasively proliferative cells that drive synovitis. Both THY1- and THY1+ FLS share many characteristics with fibroblast-like progenitors – mesenchymal stromal cells (MSC). However, it remains unclear whether synovitis-induced metabolic changes exist in FLS from OA patients and whether metabolic differences may provide a mechanistic basis for the identification of approaches to precisely convert the pathologically proliferative synovitis-driven FLS phenotype into a healthy one. To identify novel pathological mechanisms of the perpetuation and manifestation of OA, we analyzed metabolic, proteomic, and functional characteristics of THY1+ FLS from patients with OA. Proteome data and pathway analysis revealed that an elevated expression of pyruvate dehydrogenase kinase (PDK) 3 was characteristic of proliferative THY1+ FLS from patients with OA. These FLS also had the highest podoplanin (PDPN) expression and localized to the sublining but also the lining layer in OA synovium in contrast to the synovium of ligament trauma patients. Inhibition of PDKs reprogrammed metabolism from glycolysis towards oxidative phosphorylation and reduced FLS proliferation and inflammatory cytokine secretion. This study provides new mechanistic insights into the importance of FLS metabolism in the pathogenesis of OA. Given the selective overexpression of PDK3 in OA synovium and its restricted distribution in synovial tissue from ligament trauma patients and MSC, PDKs may represent attractive selective metabolic targets for OA treatment. Moreover, targeting PDKs does not affect cells in a homeostatic, oxidative state. Our data provide an evidence-based rationale for the idea that inhibition of PDKs could restore the healthy THY1+ FLS phenotype. This approach may mitigate the progression of OA

and thereby fundamentally change the clinical management of OA from the treatment of symptoms to addressing causes.

Graphical Abstract

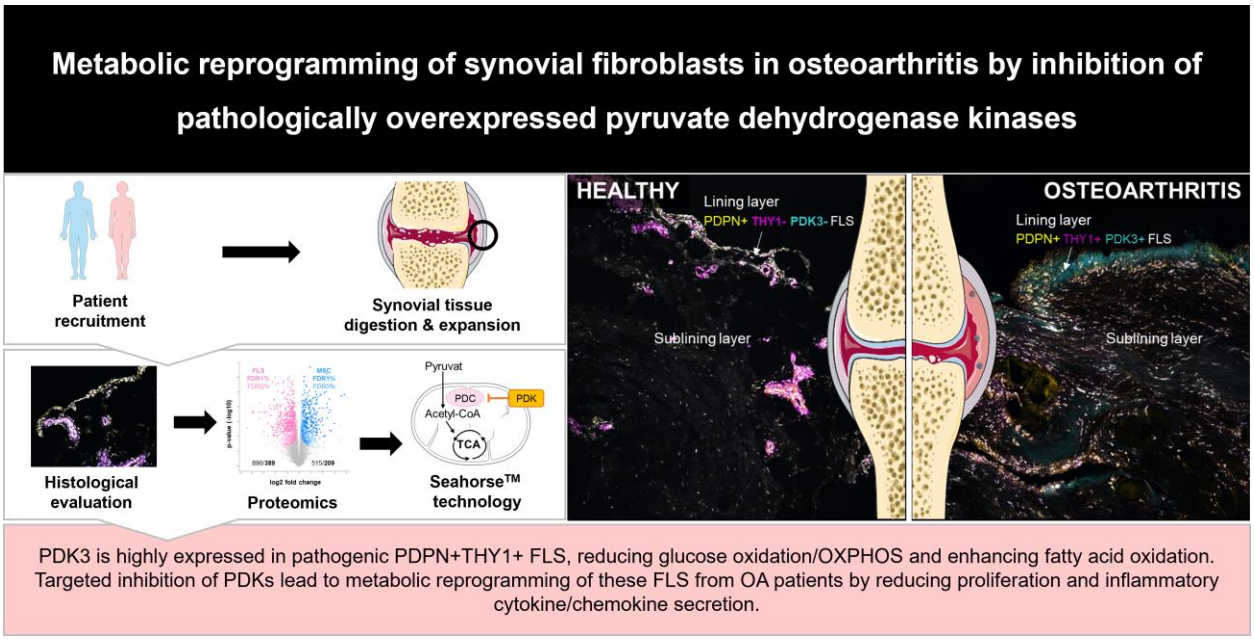

Keywords

synovial fibroblasts, THY1, mesenchymal stromal cells, metabolism, synovitis, proteomics, metabolic engineering

Introduction

Osteoarthritis (OA) is the most common age-related degenerative joint disease affecting more than 500 million people worldwide in 2019, with women being disproportionately more frequently affected by the condition (Hunter et al., 2020). To date, OA remains the leading cause of joint pain and age-related disability. OA was initially classified as a non-inflammatory joint disease – a consequence of early observations based on the relative lack of neutrophils in the synovial fluid and the absence of a systemic inflammatory manifestation compared with rheumatoid arthritis (RA) (Berenbaum, 2013; Sokolove and Lepus, 2013). However, the complex pathogenesis of OA involves a diverse interplay between various humoral factors, cell types, and tissues, characterized by progressive articular cartilage degradation, thickening of the subchondral bone, development of osteophytes, fibrosis, and synovitis (Mathiessen and Conaghan, 2017; Wang et al., 2018). Synovitis has been recognized as the main driver of joint pain for a long time (O'Neill and Felson, 2018). Recently, attention has been drawn to the underlying mechanisms of synovitis in the multifactorial etiology of OA.

Fibroblast-like synoviocytes (FLS) were identified as key drivers of inflammatory joint destruction in OA (Bhattaram and Chandrasekharan, 2017; Muller-Ladner et al., 2007). Based on single-cell RNA sequencing (scRNA-seq) data from RA and OA synovial tissue biopsies, FLS have been functionally divided into two major populations based on the expression of thymus cell antigen 1 (THY1, CD90) (Cai et al., 2019; Croft et al., 2019; Mizoguchi et al., 2018). The THY1- destructive FLS phenotype is restricted to the synovial lining layer, may stimulate osteoclastogenesis via Receptor Activator of NF-κB Ligand secretion, and has been assumed to promote bone erosion under pathological conditions. In contrast, THY1+ FLS of the sublining layer have been classified as invasive proliferative cells with immune effector function that secrete proinflammatory cytokines and thus drive synovitis (Cai et al., 2019; Croft et al., 2019; Mizoguchi et al., 2018). ScRNA-seq from RA synovial tissue has revealed that proliferative and thus metabolically more active THY1+ FLS are characterized by increased glycolysis and diminished but intact oxidative phosphorylation (OXPHOS) compared with non-invasive, quiescent THY1- FLS (de Oliveira et al., 2019;

McGarry and Fearon, 2019; Mizoguchi et al., 2018). Comparative analyses between FLS from patients with RA or OA and inflammation-unexposed cells such as mesenchymal stromal cells (MSC) or unexposed FLS are scarce. Pathologically altered cell metabolism, including increased glycolytic enzymes and intermediates, has been attributed to joint inflammation and disease progression in RA (Masoumi et al., 2020), while OA tissue often served as a control. Inhibition of essential glycolytic enzymes such as hexokinase 2 (HK2) by the use of 2-deoxyglucose has been shown to change the phenotype of RA FLS by reducing the secretion of proinflammatory cytokines, invasiveness, cell proliferation, and migration rate *in vitro* (Bustamante et al., 2018; Garcia-Carbonell et al., 2016). Inactivation of glycolysis further attenuated bone and cartilage damage in a model of RA (Abboud et al., 2018; Bustamante et al., 2018; Garcia-Carbonell et al., 2016).

While the introduction of disease-modifying antirheumatic drugs has revolutionized the treatment of RA (Smolen et al., 2020), OA therapy is still limited to pain control, physiotherapy, and arthroplasty in severe cases (Pendleton et al., 2000). Therefore, a better understanding of the pathogenesis of OA considering the well-established pathomechanisms of RA might facilitate the identification of pathomechanisms that may serve as potential novel therapeutic targets.

We hypothesize that synovitis-induced metabolic imbalances mark chronic local inflammation-exposed FLS from patients with OA. We assume that this imbalance cumulates in a pathological proliferative, prolific, inflammatory, and metabolically active phenotype (THY1+ FLS) that differs from inflammation-unexposed FLS/MSC. The identification of metabolic differences will provide new insights into pathomechanisms which will finally allow identifying potential novel therapeutic targets for developing disease-modifying osteoarthritis drugs (DMOADs), ultimately mitigating cartilage degeneration.

As a source for inflammation-unexposed FLS, we used phenotypically indistinguishable bone marrow-derived MSC, not exposed to direct chronic or acute inflammation since the use of FLS from healthy patients as the best inflammation-unexposed control is not justifiable for ethical reasons (Denu et al., 2016; Ugurlu and Karaoz, 2020). We compared MSC with FLS from patients with OA regarding the phenotype, differentiation, proliferation, and metabolism and with FLS from patients with ligament trauma regarding

proliferation and cytokine/chemokine secretion. We confirmed these cells as fibroblast-like, inflammation-unexposed control cells. In this context, the use of mass spectrometry-based shotgun proteomics allowed for global quantitative protein expression profiling: We newly identified an enhanced expression of pyruvate dehydrogenase kinase (PDK) isoforms in active proliferative and prolific PDPN+THY1+ FLS from patients with OA. PDKs inhibit the pyruvate dehydrogenase (PDH) complex by preventing the decarboxylation of pyruvate, thereby limiting its entry into the tricarboxylic acid (TCA) cycle and thus the electron flux via the electron-transport chain, finally reducing mitochondrial ATP production (Woolbright et al., 2019). By inhibiting PDK activity, we confirmed its pathogenic role as a gatekeeper for cell metabolic processes and fibroblast proliferation and secretion of inflammatory cytokines. Microanatomy of the synovial tissue was histologically analyzed to visualize the spatial distribution of PDK3 and the different FLS phenotypes in the lining and sublining layer. In contrast to previous reports (Abuwarwar et al., 2018; Croft et al., 2019), we identified an abnormal high abundance of PDPN+THY1+ FLS in the lining layer with the majority of PDPN+ cells localized in both the synovial lining and sublining layer in the OA synovium. Finally, we performed pathway analyses to identify metabolic alterations and functional experiments to determine the potential of targeted inhibition of PDKs in OA to develop DMOADs.

Given the selective abnormal overexpression of PDK3 in OA synovium and its restricted distribution in synovial tissue from ligament trauma patients, especially PDK3 represents the distinct mechanistic difference between health and disease to serve as an attractive selective target for OA therapy without affecting cells being in a homeostatic, oxidative state such as observed for non-inflammatory MSC or low-grade inflamed FLS from patients with ligament injuries. Thus, this approach might be safer than global inhibition of glycolysis using, e.g.,2-DG.

Material and Methods

Tissue and ethics statement

Human bone marrow-derived MSC were obtained from patients undergoing total hip replacement (provided by the Center of Musculoskeletal Surgery, Charité–Universitätsmedizin Berlin and distributed via the

"Tissue Harvesting" core facility of the BCRT, donor list in Supplementary Table 1). As previously described, MSC isolation and characterization (Damerau et al., 2020). FLS were isolated from (i) tibial plateau samples excised during knee arthroplasty for OA and (ii) synovial tissue sections from trauma patients collected during anterior cruciate ligament (ACL) reconstruction for an ACL rupture (provided by the Center of Musculoskeletal Surgery, Charité–Universitätsmedizin Berlin, donor list in Supplementary Table 1). Study design and protocols were approved by the Charité–Universitätsmedizin Ethics Committee and performed according to the Helsinki Declaration (ethical approval EA1/012/13, January 2013, EA1/146/21, May 2021).

Digestion of the synovium and culture of FLS

The synovium was dissected and separated from fat tissue as fat can compromise the viability of isolated cells. After washing the tissue with 0.5% bovine serum albumin (Sigma-Aldrich) and 5 mM EDTA in phosphate-buffered saline (PBS/BSA/EDTA; pH 7.4), the tissue was transferred into a 15 ml tube containing digestion buffer: DMEM GlutaMAX™ (Gibco) supplemented with 1U Liberase TL (Roche) and 100 µg/ml DNAse (Roche). Subsequently, the tube was incubated at 37°C for 45 min in a MACSmix™ Tube Rotator (Miltenyi Biotech). Samples were transferred to a 75 cm^2 flask and incubated in DMEM supplemented with 10% fetal calf serum (FCS; Biowest), 100 µg/ml penicillin (Gibco), and 100 µg/ml streptomycin (Gibco), in the following referred to as normal medium (NM) in a humidified atmosphere (37°C, 5% CO_2).

Antibodies

Staining for flow cytometry was performed using antibodies from Miltenyi Biotec against CD73-APC (REA804), CD90-FITC (REA897), CD105-APC-Vio770 (REA794), CD14-PE (REA599), CD20-PE (REA780), CD34-PE (REA1164), CD45-PE (REA747), HLA-DR-PE (REA805), PDPN-PE (REA446), CD10-PE-Vio770 (REA877), CD26-APC (FR10-11G9). Isotype control antibodies (Miltenyi Biotec) were utilized to verify the staining. Antibodies against Vimentin-A488 (monoclonal, EPR3776, 1:200, ab185030, Abcam), Collagen type 1 (unconjugated, monoclonal, IgG1, 1:200, ab6308, Abcam), THY1-A568

(monoclonal, EPR3133, 1:100, ab201848, Abcam), PDK3 (unconjugated, polyclonal, IgG, 1:200, Thermo Fisher Scientific), PDPN (unconjugated, monoclonal, NC-08, 1:200, BioLegend), pPDHA1 [p Ser293] (Alexa 488, polyclonal, IgG, 1:200, NB110, Novus Biologicals), Ki67 (unconjugated, polyclonal, IgG, 1:1000, ab15580, Abcam), MitoTracker™ Green FM (1:100, Thermo Fisher Scientific) and the secondary antibodies goat anti-rat A647 (1:500, Thermo Fisher Scientific), goat anti-mouse A546 (1:500, Thermo Fisher Scientific), goat anti-rabbit A546 (1:500, Thermo Fisher Scientific), and donkey anti-rabbit A488 (1:500, Thermo Fisher Scientific) were used for immunofluorescence analysis. Isotype control antibodies were utilized to verify the staining: Recombinant Alexa Fluor® 568 Rabbit IgG isotype control (monoclonal, EPR25A, ab209613, Abcam), purified Rat IgG2a, λ isotype control (monoclonal, G013C12, BioLegend), and rabbit IgG isotype control (Thermo Fisher Scientific).

Alizarin Red S assay

Alizarin Red S assay was performed for calcium quantification as previously described (Pfeiffenberger et al., 2020) and quantified at 562 nm (reference wavelength 630 nm). In brief, cells were differentiated using StemMACS™ OsteoDiff medium (Miltenyi Biotech) and normalized to cells in NM. The assay was performed in duplicates.

Proliferation, viability, cytotoxicity assay

Assays were performed according to the manufacturer's instructions. $1x10^4$ cells per well were seeded in a flat bottom 96-Well plate (Greiner Bio-one). Proliferation was assessed using the Cell Proliferation ELISA, BrdU (colorimetric) assay (Roche), Thymidine Incorporation assay (Thermo Fisher Scientific), and cell count via Neubauer Chamber (Sigma-Aldrich). Cells were treated with 1 µg/ml actinomycin D (neg ctrl) to suppress transcription and thus proliferation. Viability was analyzed using the Cell Proliferation Reagent WST-1 Kit (Sigma-Aldrich). Samples were mixed with WST-1 solution and incubated for 2 h at 37°C, 5% CO_2. Cytotoxicity Detection LDH Kit (Sigma-Aldrich) was used to detect cytotoxic effects of DCA (0.5, 1, 5, 10, and 25 mM) after 24 h at 37°C, 5% CO_2. In addition, to induce LDH release via cell death, cells were incubated with 2% Triton X-100 (Sigma-Aldrich) for 24 h (high ctrl).

Proteome analysis

Cell pellets were resuspended in SDC buffer (1% Sodium deoxycholate, 100 mM Tris-HCl pH 8, 1 mM EDTA, 150 mM NaCl, 10 mM dithiothreitol, 40 mM Chloroacetamide), heated for 10 minutes at 95°C, cooled down to RT, and incubated with 25 U Benzonase (Merck) for 30 minutes. After centrifugation for 20 minutes at 400 x *g*, protein extracts were collected and subjected to tryptic digestion. To each sample (100 µg protein) 2 µg sequence-grade Trypsin (Promega) and 2 µg Lysyl Endopeptidase LysC (Wako) was added and incubated overnight at 37°C. The digestion was stopped by adding trifluoroacetic acid (final concentration 1%), and peptides were desalted and cleaned up using StageTips protocol (Rappsilber et al., 2003). Peptide samples were eluted from StageTips (80% acetonitrile, 0.1% formic acid), and after evaporating the organic solvent, peptides were resolved in sample buffer (3% acetonitrile/ 0.1% formic acid). Two analytical runs using 1 µg of peptide material were performed for each replicate. Peptides were separated on a 20 cm reversed-phase column (75 µm inner diameter, packed with ReproSil-Pur C18-AQ (1.9 µm, Dr. Maisch GmbH) using a 200 min gradient with a 250 ml/min flow rate of increasing Buffer B concentration (from 2% to 60%) on a High-Performance Liquid Chromatography system (Thermo Fisher Scientific). Peptides were measured on a Q Exactive Plus Orbitrap instrument (Thermo Fisher Scientific). The mass spectrometer was operated in the data-dependent mode with a 70K resolution, 3 x 10^6 ion count target, and maximum injection time of 120 ms for the full scan, followed by Top 10 MS2 scans with 17.5K resolution, 1x10^5 ion count target, and maximum injection time of 60 ms. Dynamic exclusion was set to 30 sec. Raw data were processed using the MaxQuant software package (v1.6.3.4) (Tyanova et al., 2016) and a decoy human UniProt database (HUMAN.2019-07), containing forward and reverse sequences. The search included variable modifications of oxidation (M), N-terminal acetylation, deamidation (N and Q), and fixed modification of carbamidomethyl cysteine. Minimal peptide length was set to six amino acids, and a maximum of two missed cleavages was allowed. The FDR was set to 1% for peptide and protein identifications. Unique and razor peptides were considered for quantification. MS2 identifications were transferred between runs with the "Match between runs" option. The integrated LFQ (label-free) quantitation algorithm was applied.

Reverse hits, contaminants, and proteins identified by site were filtered out, and statistical data analysis was performed using the Perseus software (v 1.6.2.1). For statistical analyses, 5 biological replicates for each condition (FLS and MSC) were defined as groups, and a minimum of 3 LFQ intensity values in at least one group was required. Missing values were imputed with low-intensity values simulating the detection limit of the mass spectrometer. Differences in protein abundance between the groups were calculated using the two-sample Student´s t-test. Proteins passing the FDR-based significance cut-off (1 and 5%) were considered differentially expressed. GO enrichment analysis was performed in Perseus with a background set of all detected proteins. Terms were filtered for p-value (corrected) <0.02, number of proteins in category (set size) >2. Reduction of terms was achieved using REVIGO with the following settings: medium reduction, against the *homo sapiens* database, SimRel similarity measure, and without an order of terms (Supek et al., 2011). Complete proteome data are available via ProteomeXchange with identifier PXD027215.

Metabolic analysis using Seahorse^{TM} technology

Metabolic characterization was performed using a Seahorse XFe96 Extracellular Flux Analyzer (Seahorse Bioscience). Briefly, $1x10^5$ cells were seeded into the Seahorse XF Cell Culture Microplate (Agilent Technology). For analysis, cells were resuspended in XF assay media (Agilent Technology) supplemented with 10 mM glucose (Sigma-Aldrich), 1 mM pyruvate (Sigma-Aldrich), and 2 mM glutamine (Sigma-Aldrich). The Cell Mito Stress Test was performed using 2 µM oligomycin, 1.5 µM FCCP (carbonyl cyanide-p-trifluoromethoxy-phenyl-hydrazone), 0.5 µM rotenone, and 0.5 µM antimycin A (RotAA) purchased from Agilent Technologie. The Glycolytic Rate Assay was performed using 0.5 µM RotAA and 50 mM 2-Deoxy-D-glucose (Sigma-Aldrich), and purchased from Agilent Technologies. Mitochondrial stress and glycolytic parameters were measured via OCR in pmol/min/$1x10^5$ cells. Metabolic parameters were calculated according to the manufacturer's instructions (Agilent Technologies).

Metabolic inhibition of PDKs

DCA was applied in a 5 mM (Sigma-Aldrich) concentration with or without 4 µM etomoxir (ETO; Agilent Technologies) to cells seeded in the Seahorse XF Cell Culture Microplate and incubated for 2 h at 37°C in a non-CO_2 incubator.

ATP measurement

Intracellular ATP levels were measured using the ATPlite 1step Luminescence Assay System (Perkin Elmer), a method based on the reaction of ATP with luciferase and D-luciferin. $1x10^5$ cells per well (duplicates) were seeded in Corning® flat bottom, black 96-Well plates (Sigma-Aldrich). Luminescence was measured with a Spectra Max Gemini EM luminescence microplate reader (Molecular Devices) and normalized to background levels.

Glucose and lactate analysis

Glucose and lactate contents were measured using the Biosen C-line analyzer (EKF Diagnostic). $1x10^5$ cells per well (triplicates) were seeded in 12-Well plates (Greiner Bio-one) and cultured in DMEM without FCS (Ctrl) or treated with 5 mM DCA for up to 7 days (37°C, 5% CO_2).

Cytokine and chemokine quantification in cell culture supernatants

Cell culture supernatants were immediately stored at −80 °C. The concentration of cytokines and chemokines in pg/ml per $5*10^3$ cells was determined according to the manufacturer's instructions using the multiplex suspension assay (Bio-Rad Laboratories). The following cytokines and chemokines (lower detection limit) were measured: interleukin (IL)-6, IL-8, tumor necrosis factor (TNF)α, vascular endothelial growth factor A (VEGFA), granulocyte-macrophage colony-stimulating factor (GM-CSF), monocyte chemotactic protein-1 (MCP-1)/ Chemokine (C-C Motif) Ligand (CCL) 2, macrophage inflammatory protein (MIP)-1α/CCL3 and MIP-1β/CCL4.

Flow cytometry analysis

Flow cytometry staining was performed on ice in U-bottom 96-Well plates (Greiner Bio-one) using a combination of the antibodies mentioned above. After blocking the unspecific binding of Fc-receptors using

a solution containing 5 mg/ml human IgG (IgG1 66.6%, IgG2 28.5%, IgG3 2.7%, IgG4 2.2%; Flebogamma, Grifols), cells were washed in PBS/BSA/Azide, and antibody staining was performed for 15-20 min according to the manufacturer's instructions. Cells were washed and centrifuged at 400 x *g* for 4 min and resuspended in PBS/BSA/Azide. Shortly before analysis, cells were incubated with 1 µg/ml 4′,6-diamidino-2-phenylindole (DAPI; Sigma-Aldrich) for 2 min at RT to exclude dead cells.

Samples were measured using a MACS Quant Analyzer 10 (Miltenyi Biotec) and analyzed with FlowJo™ software (version 7.6.4 and 10.7.1, Tree Star). The gating strategy is depicted in Supplementary Fig. 1 and Supplementary Fig. 2.

Immunofluorescence staining

Immunofluorescence staining was performed in the dark at RT. Cells were fixed with 4% paraformaldehyde (PFA; Electron Microscopy Sciences) for 8 min, washed with PBS (3x1 min), and permeabilized using PBS/0,1% Tween®20 (Qbiogene Inc.) for 10 min. Subsequently, unspecific binding sites were blocked with PBS/5% FCS for 30 min. Afterward, the primary antibody was diluted in PBS/5% FCS/0.1% Tween®20 and incubated according to the manufacturer's instructions, followed by washing with PBS/0.1% Tween®20 (3x1 min). The secondary antibody was diluted in PBS/5% FCS/ 0.1% Tween®20 and applied for 2 h, washed with PBS/0.1% Tween®20 (3x1 min) and nuclei staining was performed using DAPI (1 µg/ml diluted in PBS/0.1% Tween®20, 15 min). Imaging was performed with the laser scanning fluorescence microscope LSM 710 (Carl Zeiss) using lasers of specific wavelengths. Image analysis was performed using FIJI ImageJ 1.52p (National Institutes of Health).

RNA isolation, cDNA synthesis, and quantitative PCR (qPCR)

Total RNA was isolated according to the manufacturer's instructions using the RNeasy® Mini Kit (Qiagen). TaqMan® Reverse Transcription Reagents Kit (Applied Biosystems Inc.) was used for cDNA synthesis. Quantification of gene expression was performed by qPCR in the Stratagene Mx3000P™ (Agilent Technologies Inc.) using the DyNAmo ColorFlash SYBR Green qPCR Kit (Thermo Fisher Scientific) according to the manufacturer's instructions. The qPCR was performed in duplicates with a non-template

control (NTC) for each master-mix using the following temperature profile: 7 min at 95°C, 60 cycles with 7 s at 60°C and 10 s denaturation at 95°C, and 9 s at 72°C. After every run, a melting curve analysis was performed to confirm primer specificity. In cases where the amplification curve did not reach the threshold within the cycles, the value of the maximum cycle number was used. Data were normalized to the elongation-factor 1-α (*EF1A*) expression using the ΔCt-method. All primers were purchased from TIB Molbiol (Table 1).

Table 1: Sequences of primers used for qPCR.

Gene	Sequence of forward primer	Sequence of reverse primer
EF1A	TGTGCTGTCCTGATTGTTGC	GTAGGGTGGCTCAGTGGAAT
PDPN	GACTCCGCTCGGAAAGTTCT	ACACCTTCCACATCGTTCCC
THY1	GACCCGTGAGACAAAGAAGC	GCCCTCACACTTGACCAGTT
VIM	GGACCAGCTAACCAACGACA	AAGGTCAAGACGTGCCAGAG
CD9	CATGCTGGGACTGTTCTTCG	GATAAACTGTTCCACGCCCC
TNC	GACAATGAGATGCGGGTCAC	CGCTGACAGGAATGCTCTTC
DCN	CCTTTGGTGAAGTTGGAACG	TCGCACTTTGGTGATCTCAT
FSP1	TCTTGGTTTGATCCTGACTGCT	TCACCCTCTTTGCCCGAGTA
FN1	GGTGACACTTATGAGCGTCCTAAA	AACATGTAACCACCAGTCTCATGTG
HAS1	GGAGATTCGGTGGACTACGT	CGCTCCACATTGAAGGCTAC
HAS2	TGTCGAGTTTACTTCCCGCC	CAGCGTCAAAAGCATGACCC
HAS3	TGTGCAGTGTATTAGTGGGCCCTT	TTGGAGCGCGTATACTTAGTT
COL1A1	CAGCCGCTTCACCTACAGC	TTTTGTATTCAATCACTGTCTTGCC
COL3A1	CTTTGTGCAAAAGGGGAGCT	TGGGTTGGGGCAGTCTAATT
SUOX	TCCCATGTGCGTGAGTTACT	AGGTACAGGCAGATGGTTCC
ICAM1	CGACTGGACGAGAGGGATTG	GATAGGTTCAGGGAGGCGTG
VCAM1	GGGAAGATGGTCGTGATCCT	TCGTCACCTTCCCATTCAGT
ITGB3	ACCAGTAACCTGCGGATTGG	TCCGTGACACACTCTGCTTC
VEGFA	AGCCTTGCCTTGCTGCTCTA	GTGCTGGCCTTGGTGAGG
SLC2A1	AACCACTGCAACGGCTTAGA	TCACGGCTGGCACAAAACTA
SLC2A3	ACCGGCTTCCTCATTACCTT	AGGCTCGATGCTGTTCATCT
LDHA	ACCCAGTTTCCACCATGATT	CCCAAAATGCAAGGAACACT
LDHB	TTGTCTTCTCCGCACGACTG	GTCCTGAGCCGAAACCTACC
PDK1	GAGAGCCACTATGGAACACCA	GGAGGTCTCAACACGAGGT
PDK2	ATGAAAGAGATCAACCTGCTTCC	GGCTCTGGACATACCAGCTC
PDK3	CGCTCTCCATCAAACAATTCCT	CCACTGAAGGGCGGTTAAGTA
CPT1A	TCCAGTTGGCTTATCGTGGTG	TCCAGAGTCCGATTGATTTTTGC
PDHA1	ATGGAATGGGAACGTCTGTTG	CCTCTCGGACGCACAGGATA
SLC7A11	GGACAAGAAACCCAGGTGGT	GCAGATTGCCAAGATCTCAAGT
HK1	CACATGGAGTCCGAGGTTTATG	CGTGAATCCCACAGGTAACTTC
SLC16A1	CTAGCTGCGTGGGTACTGG	CCGGCTGTTACCCAACTAAC

Statistical analysis

Statistical analysis was performed using the GraphPad® Prism V.8.4.1 software (La Jolla, USA). All values are shown as box plots (centerline, median; box limits, upper and lower quartiles; whiskers, maximum and minimum values; all data points) or as scatter dot plot (median) if not indicated otherwise. Mann-Whitney U test was applied for independent datasets, while dependent datasets were compared by means using the Wilcoxon-signed rank test t (*$p<0.05$, **$p<0.01$, ***$p<0.001$) if not indicated otherwise.

Results

FLS from patients with ligament injuries demonstrate THY1+ FLS prevalent around blood vessels, while inflammation-unexposed MSC show a similar cytokine and chemokine pattern

Hypothesizing that chronic local inflammation induces metabolic imbalances in FLS which lead to a proliferative, prolific, inflammatory, and metabolically-active phenotype, we analyzed the expression of THY1 – the marker to distinguish proliferative THY1+ and quiescent THY1- FLS – in synovial tissue sections from patients with OA compared with synovial tissue sections from trauma patients without signs of chronic inflammation (e.g., patients undergoing ACL reconstruction for an ACL rupture). Synovial tissue sections from OA patients demonstrate THY1+ FLS in the lining and the sublining layer, whereas THY1+ FLS from trauma patients were restricted to the synovial sublining layer close to capillary structures (Fig. 1A).

To completely rule out any inflammatory effects caused by low-grade acute inflammation, we compared FLS from patients with ligament injuries with their progenitor cells, MSC, not exposed to local inflammation analyzing their cytokine/chemokine release and proliferation rate (Fig. 1B, Fig. 1C). Although we observed specific levels of the proinflammatory cytokines IL-6, IL-8, TNFα, and GM-CSF, as well as the chemokines CCL2, CCL3, CCL4, and the proangiogenic VEGFA, we confirmed a similar secretion pattern in both cell types (Fig. 1B). However, we would like to stress that the bone marrow-derived MSC we used, were obtained from patients with OA who have low-grade systemic inflammation, similar to FLS from patients with ligament injuries who have low-grade acute inflammation (due to both

the injury and the surgery). Thus, both, source of cells and surgical intervention may explain these low levels for IL-8, TNFα, and the chemokines CCL2, CCL3, and CCL4. Of note, IL-6, GM-CSF, and VEGFA are known to be abundantly expressed by MSC presumably for maintenance, self-renewal, proliferation, migration, and maintenance of oxygen supply (Ayala-Cuellar et al., 2019; Najar et al., 2021; Ullah et al., 2015). Moreover, the proliferation rate of both cell types was also similar (Fig. 1C). These data indicate that neither FLS from ligament trauma patients nor MSC from OA patients demonstrate signs of inflammation or contribute to inflammation and tissue expansion.

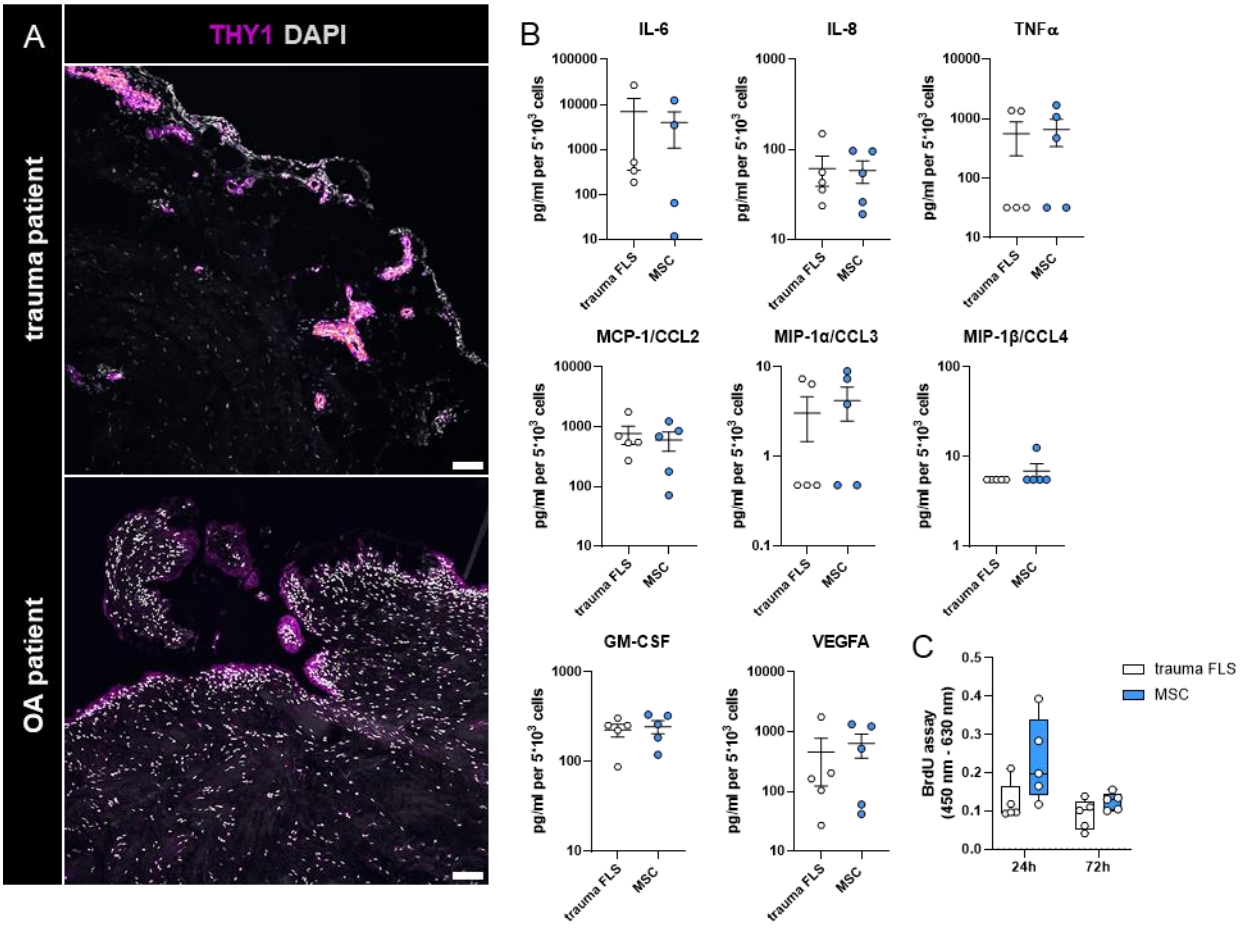

Fig. 1. Cellular localization and spatial distribution of THY1+ FLS in synovial tissue sections from both patients with OA and trauma without signs of chronic inflammation (trauma FLS) and cytokine and chemokine patterns compared with inflammation-unexposed progenitor cells (MSC). (*A*) Confocal microscopy of OA and trauma synovium (both representative of n=5). DAPI: gray, THY1: magenta. Scale bars show 100 µm. (*B*) $5*10^3$ cells of MSC and FLS from trauma patients were cultured in a 24-well plate at 37 °C and 5% CO_2. Supernatants were collected after 72 hours and analyzed via multiplex cytokine detection assay. (*C*) After 24 hours and 72 hours, a BrdU assay was conducted to explore the proliferation rate (n=5) of trauma FLS and MSC. Data in *B* are shown as scatter dot plots box plots (mean with SEM) and for *C* as box plots (centerline, median; box limits, upper and lower quartiles; whiskers, maximum and minimum values; all data points). Statistics: Two-tailed Mann-Whitney U test.

FLS from patients with OA demonstrate a stem cell-like phenotype similar to MSC but have a higher proliferation rate

Since FLS are derived from MSC, they share the function of maintaining and regenerating tissue structure by means of production, accumulation, and deposition of extracellular matrix components. Both cell types can respond to various inflammatory and non-inflammatory factors secreted by activated immune cells and damaged tissues. To identify commonalities and differences between both cell types, we firstly compared phenotypic features of FLS obtained from patients with OA with non-inflammatory MSC (Supplementary Table 1) according to the minimal criteria for MSC (Dominici et al., 2006). Both FLS and MSC demonstrated plastic adherence and the characteristic slim elongated spindle-shaped cell morphology under standard culture conditions using brightfield microscopy (Fig. 2A) and the capacity to differentiate into adipocytes and osteocytes (Fig. 2B, Fig. 2C). Flow cytometric analysis revealed a similar expression pattern of CD73, THY1, and CD105 touted as stem cell markers with >90% expression within the respective populations (Fig. 2D), whereas negative markers such as CD14, CD20, CD34, CD45, and HLA-DR accounted for <8% (Supplementary Fig. 1A; gating strategy in Supplementary Fig. 1B). Analyzing the cellular vitality of both cell types, we observed a similar activity of mitochondrial dehydrogenases (WST-1 assay) within three weeks normalized to cell numbers (Fig. 2E). When comparing cell growth and proliferation of both cell types, we measured significantly higher proliferation rates in the fibroblast population from OA synovial tissue compared with the non-inflammatory MSC as determined by cell count (Fig. 2F), BrdU assay (Fig. 2G), Ki67 staining (Fig. 2H, Fig. 2I), and 3H-thymidine assay (Supplementary Fig. 3).

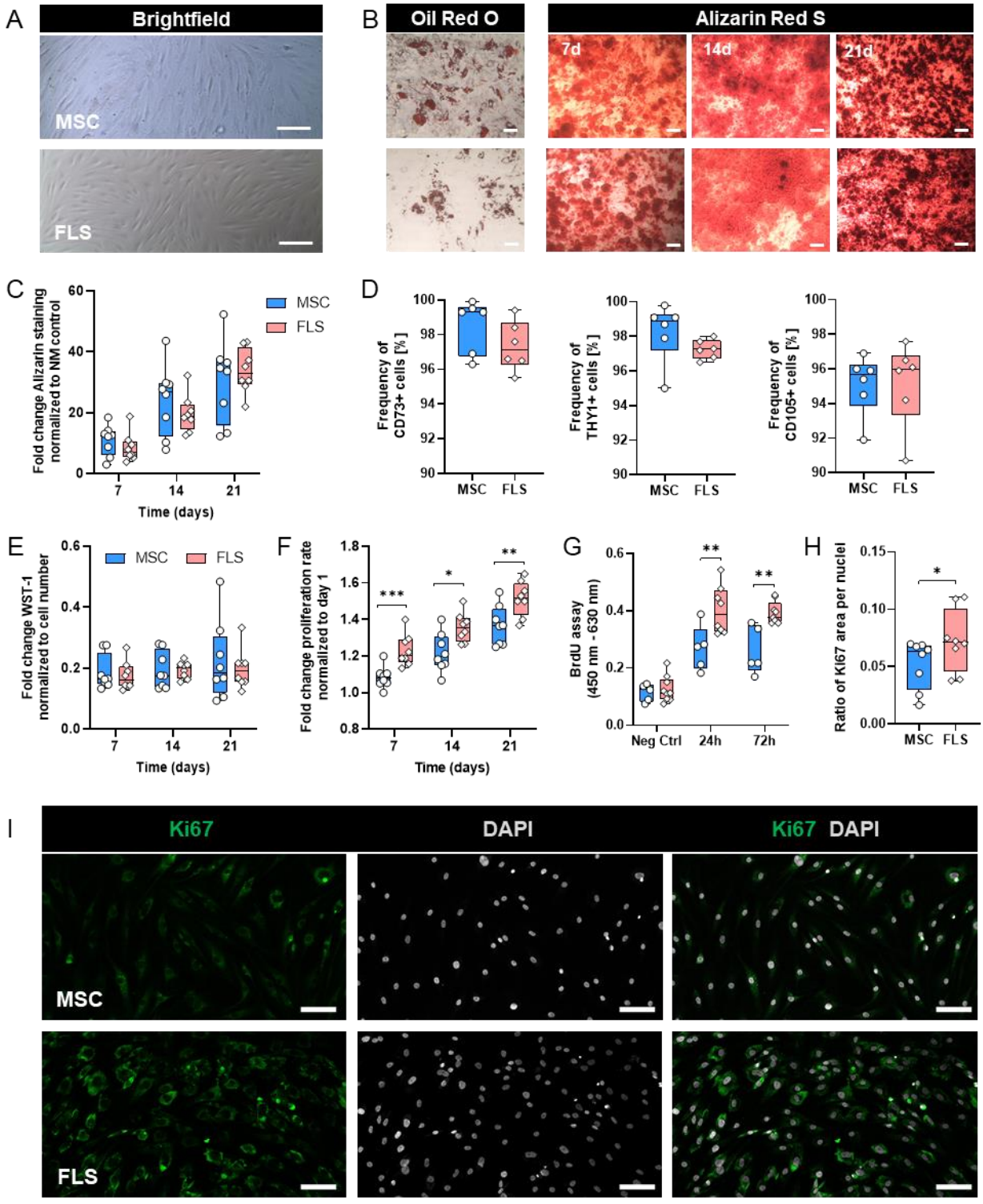

Fig. 2. FLS from patients with OA are similar to MSC in morphology and minimal criteria that define MSC, but they have a significantly higher proliferation rate. (*A*) Cells were characterized by plastic adherence, and (*B*) their differentiation capacity towards adipogenesis using Oil Red O staining and osteogenesis using Alizarin Red S staining (scale bars = 100 µm). (*C*) Alizarin Red S staining was quantified (562 nm, reference wavelength 630 nm) for n=8. (*D*) The surface expression of CD73, THY1 and CD105 was evaluated using flow cytometry (n=6). (*E*) WST-1 assay was conducted to confirm metabolically active cells after 7, 14, and 21 days of cultivation (n=8) normalized to the counted cell number. (*F*) Cells were cultivated under normoxic conditions (37°C, 5% CO_2) and counted after day 1, 7, 14, and 21 to determine the proliferation rate. (*G*) BrdU assay was conducted after 24 hours and 72 hours to analyze the proliferation rate (n=5-8). Neg Ctrl = Negative control cells treated with 1 µg/ml

actinomycin D to suppress transcription and thus proliferation. (*H*) Image quantification was performed to determine the percentage of Ki67 per nuclei (triplicates per data point) using ImageJ (n=8). (*I*) Confocal microscopy of inflammation-exposed FLS and non-exposed MSC (both representative of n=8). DAPI: gray, Ki67: green. Scale bars show 100 µm. Data are shown as box plots (centerline, median; box limits, upper and lower quartiles; whiskers, maximum and minimum values; all data points). Statistics: Two-tailed Mann-Whitney U test; p-values are indicated in the graphs with *p<0.05, **p<0.01, ***p<0.001.

Non-inflammatory MSC show a different expression pattern of PDPN, THY1, and peptidases CD10 and CD26

Mapping the distribution of distinct cell subsets within the FLS and MSC populations expanded *in vitro*, we measured the surface expression of selected fibroblast and inflammatory markers including podoplanin (PDPN), THY1, peptidase neutral endopeptidase (CD10), and dipeptidyl-peptidase IV (CD26) using flow cytometry (Fig. 3A, Fig. 3B, gating strategy in Supplementary Fig. 2). THY1 positivity was observed in more than 90% of both FLS and MSC; the number of THY1- cells was significantly higher in FLS (Fig. 3A). FLS demonstrated a significantly higher expression of PDPN. PDPN and THY1 have been reported to discriminate the FLS of the synovial lining layer (PDPN+THY1-) from FLS of the sublining layer (PDPN+THY1+) associated with different pathological functions leading to bone erosion and synovitis, respectively (Abuwarwar et al., 2018; Croft et al., 2019). *In vitro* expanded FLS show a significant subset of PDPN+THY1+ cells (83.6%) and smaller subsets of PDPN+THY1- (7.6%) and PDPN-THY1+ (5.3%) cells, representing the typical pattern of pericytes. PDPN-THY1- (2.5%) cells were almost absent (Fig. 3A). PDPN induction has been described under inflammatory conditions (Ekwall et al., 2011; Quintanilla et al., 2019). The central subpopulation of MSC (PDPN-THY1+: 66.5%) did not express PDPN. We observed a similar pattern in the transcriptome (Fig. 3C) and proteome data (Fig. 3D).

We then analyzed the surface expression of peptidases CD10 and CD26, which have been reported to be highly expressed in inflamed tissue (Nemoto et al., 1999; Ospelt et al., 2010; Solan et al., 1998) and the proliferative fibroblast subset (Ding et al., 2020; Soare et al., 2020). CD10 and CD26 were highly expressed on PDPN+THY1+ and PDPN+THY1- subpopulations of both FLS and MSC expanded *in vitro* (Fig. 3B). In PDPN-THY1+ cells, CD26 expression was significantly higher in MSC than in FLS, whereas the opposite was true for CD10. The surplus of CD10 and CD26 observed in the proteome analysis (Fig. 3D) may be attributed to the shedding of CD26 from the cell surface (Klemann et al., 2016).

However, analyses of global proteome data revealed the expected predominance of inflammatory proteins in FLS from patients with OA triggered by synovitis compared with MSC: We observed a significantly higher expression of IL-17 receptor α (IL17RA), IL-13 receptor α2 (IL13RA2), IL-1 receptor type 1 (IL1R1), and TNFα-induced protein 2 (TNFAIP2), as well as a numerically higher expression of IL-6 cytokine family signal transducer (IL6ST) and transforming growth factor beta-induced (TGFBI) protein (Fig. 3E). However, we need to consider that bone marrow-derived MSC were obtained from patients with OA. They have low-grade systemic inflammation, similar to how FLS from patients with ligament injuries have low-grade acute inflammation also due to surgery. Thus, the source of cells and surgical intervention may explain these low levels for IL-8, TNFα, and the chemokines CCL2, CCL3, CCL4, whereas IL-6, GM-CSF, and VEGFA are known to be abundantly expressed by MSC presumably for maintenance, self-renewal, proliferation, migration, and maintenance of oxygen supply.

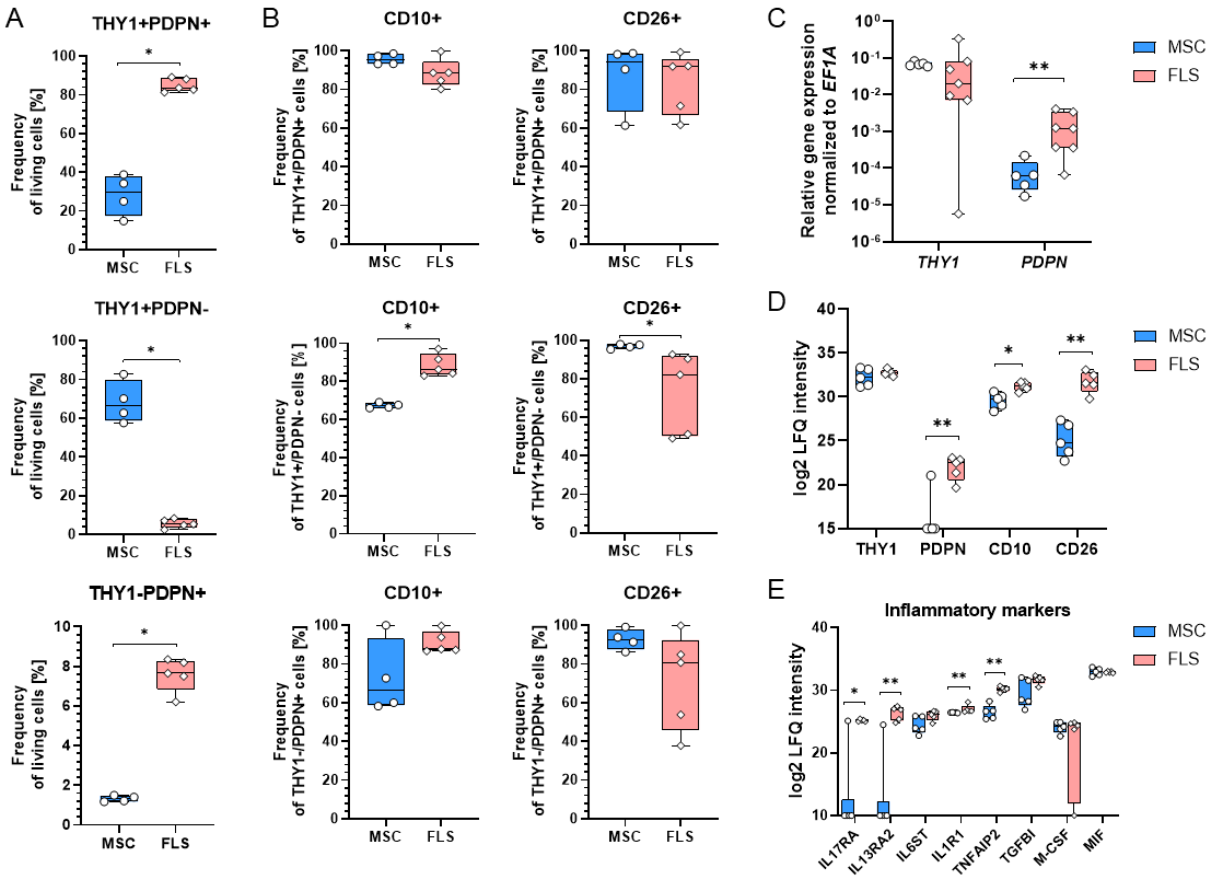

Fig. 3. The proportion of inflammation-exposed FLS subsets compared to the non-exposed MSC. (*A*) The proportion of FLS subsets in OA synovial tissue (n=5) and MSC (n=4) about THY1+PDPN+, THY1+PDPN- and THY1-PDPN+ cells were evaluated by flow cytometry. (*B*) Proportions of CD10+ and CD26+ cells in THY1+PDPN+, THY1+PDPN- and THY1-PDPN+ cells (n=3-5). (*C*) Gene expression of *THY1* and *PDPN* was normalized to the housekeeper gene *EF1A* (n=5-7). (*D*) LFQ (label-free quantitation) intensity values of the proteins THY1, PDPN, CD10, and CD26 (n=5). (*E*) LFQ intensities for 8 inflammatory markers in MSC and FLS (n=5). Data are shown as box plots (centerline, median; box limits, upper and lower quartiles; whiskers, maximum and minimum values; all data points). Statistics: Two-tailed Mann-Whitney U test; p-values are indicated in the graphs with *p<0.05, **p<0.01. Legend: M-CSF = macrophage colony stimulating factor, MIF = macrophage migration inhibitory factor.

FLS from patients with OA show different protein signatures compared with non-inflammatory MSC

A global proteome comparison of FLS and MSC revealed 592 (1405) differentially expressed proteins when applying a false discovery rate (FDR) cut-off of 1% (5%) while exhibiting a matching protein expression pattern for 90.4% (77.4%) (Supplementary Fig. 4). We found 389 (890) proteins with a significantly higher expression in FLS and 209 (515) proteins higher expressed in MSC (Fig. 4A). GO enrichment analysis for biological processes associated the majority of differentially expressed proteins (at FDR1%) to the clusters of ‘cellular component organization’ and ‘cell adhesion’ for MSC enriched proteins and to ‘tRNA metabolic process’ and ‘lipid metabolic processes’ for FLS enriched proteins (Fig. 4A, REVIGO-terms).

The inspection of expression profiles of well-established marker proteins revealed higher levels of most classical fibroblast markers in FLS than in MSC, including vimentin (VIM), tenascin c (TNC), decorin (DCN), fibroblast-specific protein 1 (FSP1), CD44, alanine aminopeptidase (ANPEP), integrin beta 3 (ITGB3), and CD9 (Fig. 4B). Conversely, stem cell-related markers such as melanoma cell adhesion molecule (MCAM; CD146), integrin subunit alpha 11 (ITGA11), and beta 1 (ITGB1) showed a lower protein expression in FLS than in MSC. Notably, the expression of fibroblast-related fibronectin 1 (FN1) was lower in FLS than in MSC, while the opposite was true for stem cell-related Ecto-5'-nucleotidase (NT5E; CD73) and intercellular adhesion molecule 1 (ICAM1; CD54) (Fig. 4B).

Immunofluorescence microscopy confirmed protein expression of vimentin (Fig. 4C). Using the same approach, we looked at collagen type 1 and observed a higher expression in MSC (Fig. 4C). For a subset of genes, we analyzed the expression on a transcriptional level (Fig. 4D). Protein expression data were not entirely congruent with gene expression data. While *FSP1*, *FN1*, *CD9*, *ICAM1*, collagen type 1 alpha 1 (*COL1A1*), and CD44 showed good agreement of differential expression on the transcriptome and proteome level, congruency was limited concerning *VIM*, *TNC*, and *DCN* where differences in expression could not

be detected on the transcriptional level (Fig. 4D with Fig. 4B). These findings emphasize the importance of different methodological approaches to identify deviations in the expression and functionality of cellular markers.

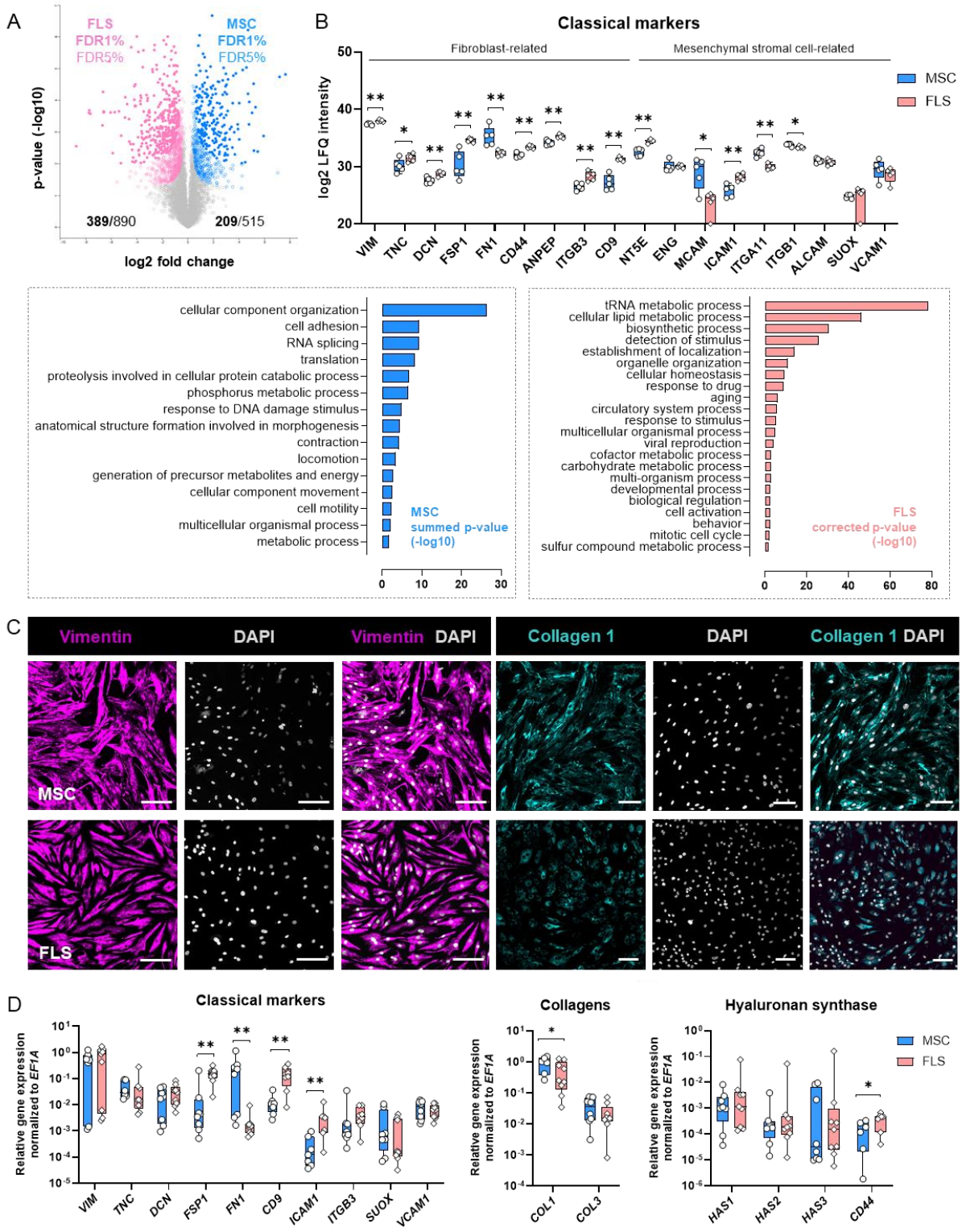

Fig. 4. Distinct protein and mRNA expression between inflammation-exposed FLS and non-exposed MSC. (*A*) Volcano plot of proteome data (LFQ intensities) comparing synovial fibroblasts (FLS, red) and mesenchymal stromal cell (MSC, blue) The colored dots indicate significant differentially expressed proteins (false discovery rate (FDR) of 1% (bold) and 5% cut-off, S0 of 0.1). GO enrichment analysis for biological processes of FLS (red) and MSC (blue) enriched proteins (FDR1% significant). REVIGO-terms and their corresponding corrected p-values (-log10 transformed) are shown as bar graphs. (*B*) Protein abundance of classical fibroblast- and MSC-related markers (n=5). Shown are log2 transformed

LFQ intensity values. (*C*) Representative images for vimentin (magenta), collagen type 1 (cyan), and DAPI (gray) are shown. Scale bars show 100 µm (n=5). (*D*) Total RNA extraction was performed from MSC and FLS. Gene expression of classical markers, collagens, and hyaluronan synthase-related genes was performed using SYBR Green and normalized to the housekeeper gene *EF1A*. *B, D* are shown as box plots (centerline, median; box limits, upper and lower quartiles; whiskers, maximum and minimum values; all data points). Statistics: Two-tailed Mann-Whitney U test; p-values are indicated in the graphs with *p<0.05, **p<0.01. Legend: ENG = endoglin, CD105; ALCAM = activated leukocyte cell adhesion molecule, CD166; SUOX = sulfite oxidase; VCAM1 = vascular cell adhesion molecule 1, CD106; HAS = Hyaluronan synthase.

FLS from patients with OA show a higher PDK3 expression than non-inflammatory MSC

We observed an enrichment of GO-terms involving metabolic processes, such as RNA metabolic process, macromolecule metabolic process, and cellular lipid metabolic process in the protein data obtained from FLS (Supplementary Table 2, Supplementary Table 3). Investigating the protein expression level of metabolic genes, we identified a significantly higher expression of PDK3 in proliferative FLS compared with non-inflammatory less proliferative MSC (log_2 FC = 3.01, p-value = 0.024; Fig. 5A). mRNA expression analysis of the four PDK isoforms (PDK4 not detectable) confirmed this finding (Fig. 5B). Additionally, we visualized PDK3 in THY1+ cells using immunofluorescence (Fig. 5C). PDK3 functions as a kinase well-known to inactivate Pyruvate Dehydrogenase E1 Subunit Alpha 1 (PDHA1) by phosphorylation, thereby limiting the entry of pyruvate into the TCA cycle and mitochondrial pyruvate oxidation via OXPHOS (Wang et al., 2021). Therefore, we first visualized the inactive, phosphorylated (Ser293) Pyruvate Dehydrogenase E1 Subunit Alpha 1 (PDHA1) and its expression with PDPN expression *in vitro* (Fig. 5D). Secondly, we compared the mitochondrial oxygen consumption rate (OCR) in FLS and non-inflammatory MSC using the Agilent Seahorse™ system (Fig. 5E). FLS demonstrated a significantly lower basal respiration, non-mitochondrial respiration, proton leak, and a lower mitochondrial ATP production than MSC despite a higher spare respiratory capacity (Fig. 5E). Furthermore, FLS demonstrated a significantly higher PER/OCR ratio, indicating that glycolysis is entirely functional but less essential to feed OXPHOS (Fig. 5F). Of note, the higher spare respiratory capacity suggests a higher number of mitochondria per cell and/or more cristae per mitochondria per cell in FLS, suggesting a functional inhibition of oxidation compared to MSC. To determine the differences in the number of mitochondria in both cell types, we visualized mitochondria by immunofluorescence microscopy, confirming our cellular respiration data (Fig. 5G). Additionally, we analyzed the retention of the mitochondrial Cytopainter™ dye using flow cytometry and confirmed the higher number of mitochondria in FLS compared with MSC (Fig.

5H). These data are supported by proteomic data, identifying 45 regulated mitochondrial proteins at FDR1% (121 at FDR5%), with the majority expressed in FLS 35 out of 45 at FDR1% (99 out of 121 at FDR5%) and more mitochondrial membrane proteins expressed in FLS 16 versus 0 at FDR1% (36 versus 4 at FDR5%) (Supplementary Table 4). Interestingly, despite a lower basal OCR, FLS demonstrate a significantly higher steady-state energy load (ATP per cell) than MSC (Fig. 5I). These findings can be accounted for by the upregulation of PDK3 facilitating rapid energy production through glycolysis – a metabolic profile in line with OA's pathological proliferative fibroblast subset.

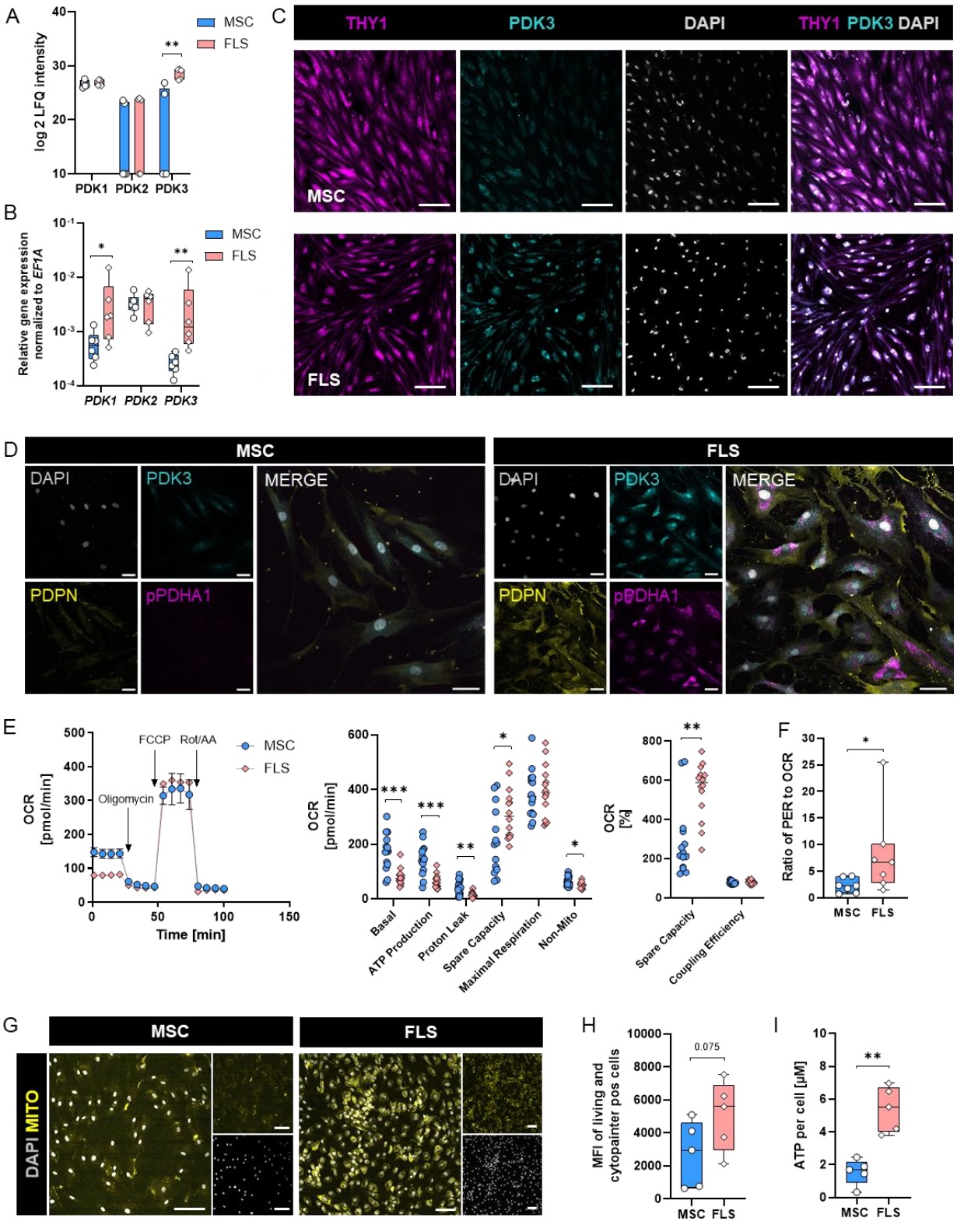

Fig. 5. PDK3 expression is up-regulated in FLS in patients with OA (*A*). Protein abundance of pyruvate dehydrogenase kinase (PDK) isoforms (n=5). log2 transformed LFQ intensity values using FDR1% significant data are shown. (*B*) Gene expression of *PDK1-3* was normalized to the housekeeper gene *EF1A*. (*C*) Representative images for THY1 (magenta), PDK3 (cyan), and DAPI (gray) are shown. Scale bars show 100 µm

(n=4). (*D*) Exemplary images for PDPN (yellow), PDK3 (cyan), phospho-(Ser293)-PDHA1 (magenta), and DAPI (gray) are shown. Scale bars show 50 µm. (*E*) Profile of Seahorse XF Mito Stress Test data for oxygen consumption rate (OCR) for non-inflammatory MSC and FLS from patients with osteoarthritis with arrows indicating injections into media of the specific stressors oligomycin, carbonyl cyanite-4 (trifluoromethoxy) phenylhydrazone (FCCP), and rotenone/antimycin A (Rot/AA). Seahorse™ technology results are shown for OCR in pmol/min per $1x10^5$ cells and percentage (n=14). Non-Mito = non-mitochondrial oxygen consumption. (*F*) Ratio of proton efflux rate (PER) to oxygen consumption rate (OCR) using Seahorse™ technology (n=7). *(G)* Representative images for Mito Tracker staining (yellow) and DAPI (gray) are shown. Scale bars show 100 µm (n=4). (*H*) Geometric mean intensity proportion of FLS and MSC concerning Cytopainter™ staining was evaluated by flow cytometry (n=5). (*I*) Intracellular ATP levels per cell were measured using the ATP-lite 1step Luminescence Assay System (n=5). Data are shown as box plots (centerline, median; box limits, upper and lower quartiles; whiskers, maximum and minimum values; all data points), except *D*, which is represented as scatter dot plot (median). Statistics: Two-tailed Mann-Whitney U test; p-values are indicated in the graphs with *p<0.05, **p<0.01, ***p<0.001.

Synovial tissue from patients with OA exhibits a marked PDK3 expression.

Since cell fate and metabolism are highly adaptive to the local microenvironment, we (i) analyzed the expression of PDK3 in synovial tissue sections from patients with OA undergoing knee arthroplasty (ii) compared these data with synovial tissue sections from trauma patients without signs of chronic inflammation, and (iii) visualized cellular localization and spatial distribution of PDK3 as well as FLS subsets in histological sections using immunofluorescence microscopy (Fig. 6, Supplementary Fig. 5).

Interestingly, most cells in OA tissue samples were PDPN+THY1+, broadly distributed in deeper sublining regions and more prominent around capillary structures but also in the synovial lining layer, which is in contrast to previous reports (Abuwarwar et al., 2018; Croft et al., 2019) (Fig. 6, Supplementary Fig. 5A). Only a few cells were PDPN+THY1-, mainly localized adjacent to the lining layer. Expression of PDK3 was observed in the majority of PDPN+THY1+ cells in both superficial lining and deeper sublining areas of the synovium, with the highest expression observed in the lining layer (Fig. 6, Supplementary Fig. 5B). Synovial tissue sections from trauma patients without signs of chronic inflammation demonstrate two distinct FLS subsets with unique spatial distribution: PDPN+THY1- FLS were confined to the lining layer, whereas PDPN+THY1+ FLS were not distributed widely in the sublining layer but were close to capillary structures. Finally, we verified our *in vitro* approach by detecting PDPN+THY1+PDK3+ FLS in *ex vivo* synovial tissue, confirming a high PDK3 expression as in PDPN+THY1+ FLS from OA patients expanded *in vitro*.

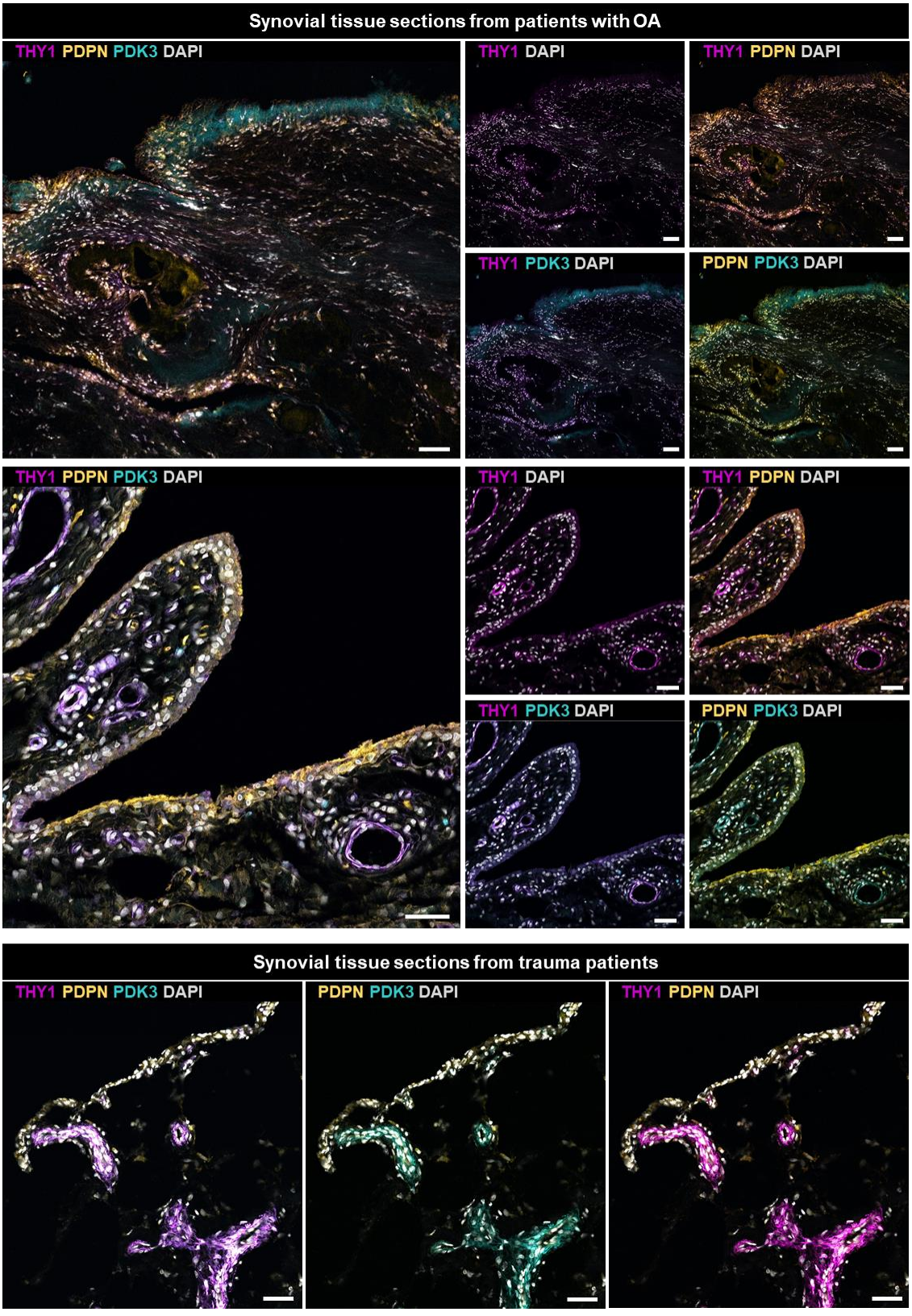

509

510 **Fig. 6.** Proportions of FLS subsets and cellular localization and spatial distribution of PDK3 in synovial tissue sections from both patients with OA
511 and trauma without signs of chronic inflammation. Confocal microscopy of OA and trauma synovium (both representative of n=5). DAPI: gray,
512 THY1: magenta, PDPN: yellow, PDK3: cyan. Scale bars show 100 µm.

Metabolic pathway analysis corresponds with high expression levels of PDK3 in OA FLS

Using *Pathview* to integrate and display proteomic data (FDR1% significant data) on KEGG pathway maps comparing FLS and non-inflammatory MSC; we first focused on proteins primarily involved in the glycolytic pathway as an ATP source (Luo and Brouwer, 2013; Luo et al., 2017). We found that proteins responsible for glucose uptake were increased in MSC compared to FLS. In contrast, enzymes that convert glucose to pyruvate, such as ADP-specific glucokinase (ADPGK) and aldolase C (ALDOC), were more abundant in FLS. This observation is consistent with the greater dependency of MSC on glycolysis and the higher PER to OCR ratio in FLS (Supplementary Fig. 6A, Supplementary Fig. 7).

Interestingly, we did not observe any differences in the transcriptional abundance of selected glycolytic genes (Supplementary Fig. 6B). Although lactate producing lactate dehydrogenase (LDH) A and its excretion transporter solute carrier family 16 member 3 (SLC16A3) were increased in MSC on protein level, an increase in the lactate to pyruvate converting enzyme LDHB and the lactate importer SLC16A1 was only observed on a transcriptional level (Supplementary Fig. 6C, Supplementary Fig. 7). Enzymes of the ethanol catabolic pathway, including alcohol dehydrogenase (ADH) 1B, ADH1C, and ADH5, were significantly increased in FLS, indicating a specific need to detoxify ethanol produced by, e.g., lipid peroxidation. (Supplementary Fig. 6C, Supplementary Fig. 7). MSC showed high levels of enzymes facilitating the metabolic conversion of pyruvate for gluconeogenesis or the TCA cycle, e.g., pyruvate carboxylase (PC) and phosphoenolpyruvate carboxykinase 2 (PCK2). In contrast, pyruvate dehydrogenase phosphatase (PDP1) – an antagonist of PDK – was more abundant in FLS (Supplementary Fig. 6D, Supplementary Fig. 7). In addition, FLS showed higher transcription of *PDHA1* – a gene encoding for the PDK target protein PDH (Supplementary Fig. 6B).

Concerning the OXPHOS related protein pattern, we did not observe significant differences in the majority of proteins identified (Supplementary Fig. 6E, Supplementary Fig. 7). However, key enzymes of mitochondrial beta-oxidation that mediate acetyl-CoA generation for the TCA cycle by catabolic break-down of long-chain fatty acid molecules showed a significantly higher expression in FLS than in MSC (Supplementary Fig. 6F, Supplementary Fig. 7). Examples include acyl-CoA:cholesterol acyltransferase

(ACAT), hydroxyacyl-CoA dehydrogenase (HADH), and acetyl-CoA synthetase (ACS). Of note, carnitine palmitoyltransferase (*CPT1A*) – the key enzyme of the carnitine-dependent transport of long-chain fatty acid molecules across the mitochondrial inner membrane – was highly expressed on transcriptional (Supplementary Fig. 6B, Supplementary Fig. 7) but not on protein level (Supplementary Fig. 6F, Supplementary Fig. 7). Similar to the OXPHOS related protein pattern, we did not observe significant differences in the majority of proteins related to the glycogen pathway (Supplementary Fig. 6G, Supplementary Fig. 7). Conversely, most identified proteins involved in the pentose phosphate pathway (PPP) were significantly more expressed in FLS than in MSC (Supplementary Fig. 6H, Supplementary Fig. 7), pointing towards an anabolic inflammatory proliferative metabolically active phenotype of the PDPN+THY1+ FLS subset. Moreover, higher expression of enzymes of the oxidative PPP branch and the glutathione metabolism in FLS indicate a reactive oxygen detoxicating phenotype (Supplementary Fig. 7, Supplementary Fig. 8) and promotion of nucleotide synthesis. In addition, cell cycle regulator proteins such as CyclinD1 showed higher expression levels in FLS supporting cell cycle progression consistent with a cancer-like phenotype (Supplementary Fig. 9, Supplementary Fig. 10). Finally, we identified an enhanced enzyme expression of the glycosaminoglycan (GAG) catabolic pathway in FLS, indicating their potential to damage the extracellular matrix (Supplementary Fig. 11).

Blocking PDK3 diminishes lactate secretion, enhances OXPHOS, and reduces the proliferative phenotype of THY1+ FLS

Based on our findings, we assumed that the high PDK3 expression in THY1+ FLS from patients with OA shifts the cells' metabolism towards glycolysis and results in a proliferative phenotype. Thus, we hypothesized that metabolic reprogramming of FLS by inhibiting PDK using dichloroacetate (DCA) reverses this phenotype (Fig. 7A). Using the LDH cytotoxicity assay, we identified a DCA concentration of 5 mM as non-lethal but effective and applied this concentration in the following experiments (Fig. 7B). Additionally, we blocked acetyl-CoA entry into the TCA cycle by incubating FLS and MSC for 2 hours with DCA alone and combined with ETO, respectively. We analyzed their OCR using Seahorse™ technology (Fig. 7C, Fig. 7D). In FLS, incubation with 5 mM DCA resulted in a significant increase in

basal respiration, ATP-linked, and acute response OCR that were all blocked in combination with ETO. In contrast, proton leak was enhanced by combined treatment with DCA and ETO, while maximal respiration and spare respiratory capacity were reduced (Fig. 7C). These effects were not seen in MSC (Fig. 7D). In addition, we observed an increase in lactate secretion over time that was attenuated by DCA treatment (Fig. 7E). Of note, glucose uptake was not affected. Finally, DCA treatment significantly reduced the transcriptional expression of *LDHB* – the enzyme converting lactate to pyruvate – and of the lactate importer *SLC16A1* as well as of the catalytic PDH complex subunit (*PDHA1*) (Fig. 7F).

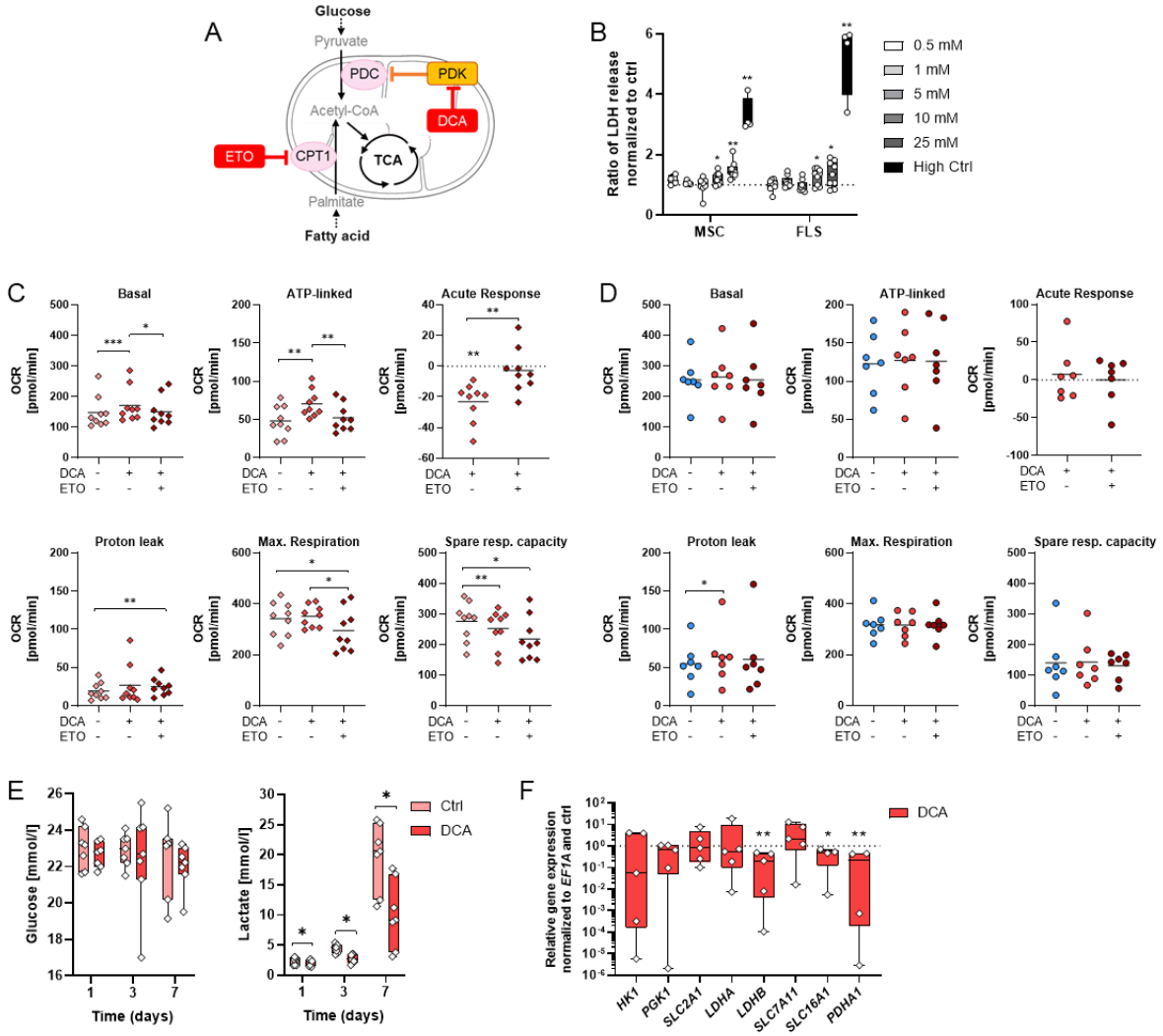

Fig. 7. PDK blockade unleashes the metabolic flux towards oxidative phosphorylation. (*A*) Schematic overview of the impact of DCA and ETO on cell metabolism. (*B*) LDH assay was performed after 24 hours and different dichloroacetate (DCA) concentrations (0.5, 1, 5, 10, and 25 mM DCA). High Ctrl = 2% Triton X-100 to induce LDH release n=4-9. (*C*) Oxygen consumption rates (OCR) are shown for synovial fibroblasts in osteoarthritis (FLS) and (*D*) mesenchymal stromal cells (MSC) treated with DCA, DCA, and ETO or left untreated (n=7-9). OCR in pmol/min using $1x10^5$ cells. (*E*) Glucose and lactate content was analyzed after day 1, 3, and 7 (n=7). (*F*) Total RNA extraction was performed from synovial fibroblasts treated with 5 mM DCA or left untreated after 3 days. Gene expression of selected pathway-relevant genes was normalized to the housekeeper gene *EF1A*

and untreated control (ctrl) for n=4-5. Data are shown as box plots (centerline, median; box limits, upper and lower quartiles; whiskers, maximum and minimum values; all data points), except *C*, *D*, which are represented as scatter dot plots (mean). Statistics: *B* Wilcoxon signed-rank test; *C*-*E* Wilcoxon matched-pairs signed-rank test; *F* one sample t-test; p-values are indicated in the graphs with *p<0.05, **p<0.01. Legend: SLC2A1 = solute carrier family 2 member 1, GLUT-1; SLC7A11 = solute carrier family 7 member 11; SLC16A1 = solute carrier family 16 Member 1, monocarboxylate transporter 1.

Having confirmed that DCA increases the metabolic flux, we investigated whether DCA-mediated metabolic reprogramming impacted the proliferation rate of FLS from patients with OA. To this end, we examined FLS proliferation with and without DCA after 24 h (Supplementary Fig. 12A) and 72 h of incubation using BrdU assay (Fig. 8A), 3H-thymidine assay (Supplementary Fig. 12B, MSC proliferation rate: Supplementary Fig. 12D, Supplementary Fig. 12E) and cell counting (Supplementary Fig. 12C). Compared with untreated FLS at baseline, we observed that DCA significantly reduced cell proliferation, indicating a potential mechanism of action that could be exploited in the form of anti-osteoarthritic drugs. Notably, the DCA-mediated reduction of cell proliferation was not accompanied by a decrease in cell survival (Fig. 8B, Fig. 8C) but by a slight decline in PDPN expression (Fig. 8D) and phosphorylation of PDHA1 (Fig. 8E). Finally, DCA treatment also reduced secreted amounts of the proinflammatory cytokines IL-6, IL-8, TNFα, and GM-CSF and for the chemokines CCL2, CCL3, CCL4, and the proangiogenic VEGFA and thus, confirmed that metabolic reprogramming of FLS from patients with OA also resets their proliferation and humoral inflammatory response to normal levels (Fig. 8F).

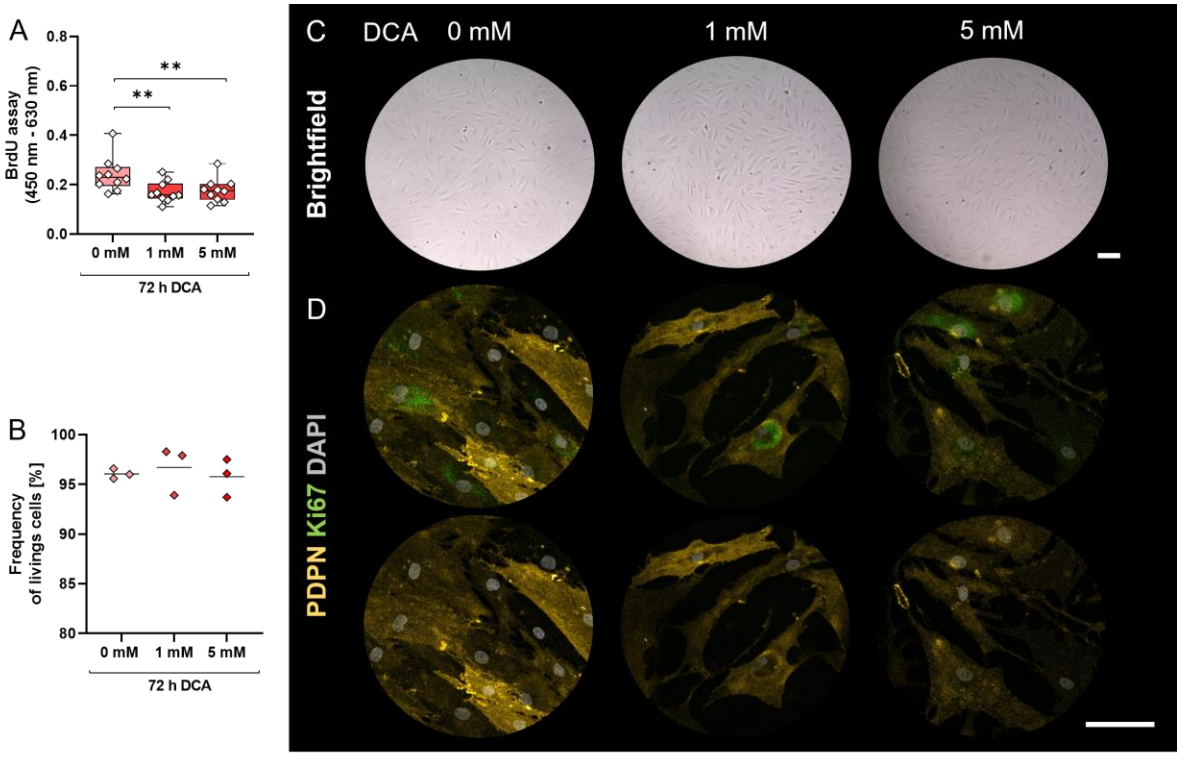
A
BrdU assay (450 nm - 630 nm)
0.8
0.6
0.4
0.2
0.0
**
**
0 mM
1 mM
5 mM
72 h DCA
B
Frequency of livings cells [%]
100
95
90
85
80
0 mM
1 mM
5 mM
72 h DCA
C
DCA
0 mM
1 mM
5 mM
Brightfield
D
PDPN Ki67 DAPI

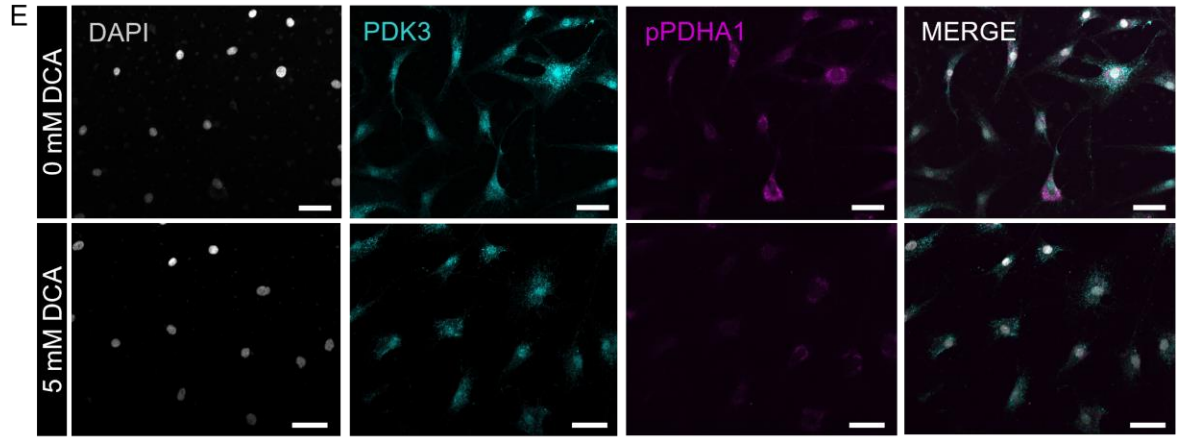
E
0 mM DCA
5 mM DCA
DAPI
PDK3
pPDHA1
MERGE

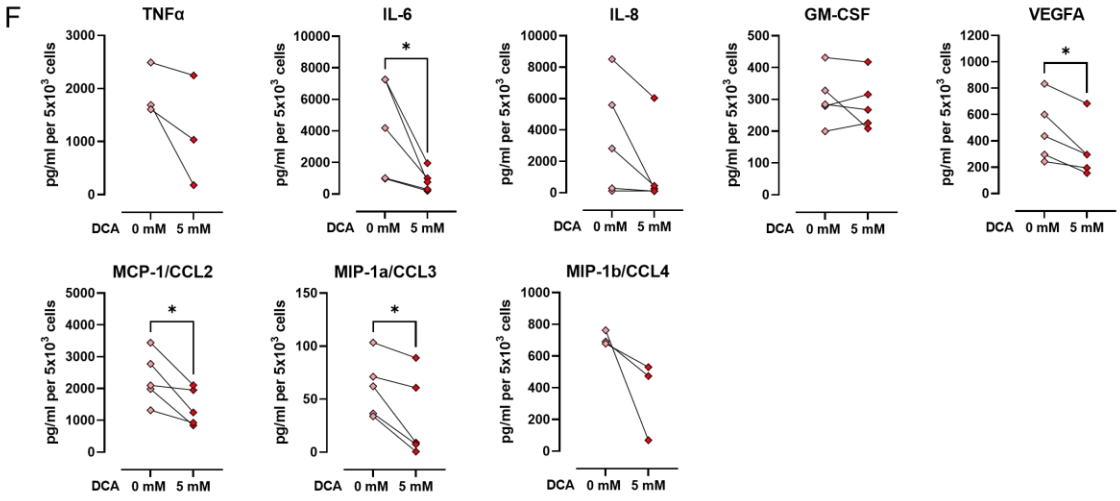
F
TNFα
IL-6
IL-8
GM-CSF
VEGFA
MCP-1/CCL2
MIP-1a/CCL3
MIP-1b/CCL4
pg/ml per 5x10^3 cells
DCA
0 mM
5 mM
*

597

Fig.8. Shifting glycolysis to OXPHOS by inhibition of PDKs results in reduced proliferation without causing cell death. (*A*) BrdU assay was conducted to analyze the proliferation rate of FLS in OA (n=10). Dichloroacetate (DCA) concentrations: 0, 1, and 5 mM. (*B*) Proportion of FLS without (0 mM) and with (1 mM and 5 mM) DCA were evaluated by flow cytometry (n=3). (*C*) Representative brightfield images of FLS cultured with or without DCA. Scale bar shows 100 µm. (*D*) Confocal microscopy of FLS with or without DCA treatment (n=3). DAPI: grey, PDPN: yellow, Ki67: green. Scale bars show 100 µm. (*E*) Representative confocal images of FLS from OA patients treated with (5 mM) and without (0 mM) DCA for 72 hours. PDK3 (cyan), phospho-(Ser293)-PDHA1 (magenta), and DAPI (grey). Scale bars show 50 µm. (*F*) Supernatants were collected after 72 hours and analyzed via multiplex cytokine detection assay. Data of *A* are shown as box plots (centerline, median; box limits, upper and lower quartiles; whiskers, maximum and minimum values; all data points), *B* is represented as scatter dot plot (mean), and *C* as before-after (symbols and lines). Statistics: Paired t-test; p-values are indicated in the graphs with *p<0.05, **p<0.01.

Discussion

Synovitis is a well-known feature of immune-mediated inflammatory joint diseases like RA. Recently, attention has been drawn to the role of synovitis in the complex pathogenesis of OA – a disease traditionally classified as a non-inflammatory degenerative joint disease (Berenbaum, 2013; Sokolove and Lepus, 2013). A metabolic shift towards glycolysis is a hallmark of inflammatory cells, whereas OXPHOS is characteristic of homeostatic and anti-inflammatory cells (Chimenti et al., 2015). Thus, we hypothesized that inflammation-exposed FLS from patients with OA are metabolically altered compared with inflammation-unexposed fibroblast-like mesenchymal control cells – bone marrow-derived MSC – leading to a pathological proliferative and glycolytically active FLS phenotype.

Although fibroblasts have recently been defined as tissue-resident MSC found in the interstitial space of all organs (Di Carlo and Peduto, 2018), we firstly confirmed THY+ MSC not affected by inflammatory stimuli as a valid fibroblast-like, non-inflammatory control (Fig. 1-3). Therefore, we showed that these MSC could not be distinguished from generic fibroblasts according to the current definition criteria for MSC (Dominici et al., 2006) (Fig. 2). Comparing FLS from OA patients with MSC about surface markers, we identified PDPN and THY1 expressed on both FLS and MSC. At the same time, a higher expression of PDPN was indicative of a fibroblast phenotype (Fig. 2). Analyzing protein expression and transcriptional response in FLS and MSC concerning so-called fibroblast and stem cell markers, we could not identify any unique characteristic marker for either cell type (Fig. 2). Secondly, FLS from patients with ligament injuries experienced by low-grade acute inflammation demonstrate a similar degree of inflammatory cytokine secretion and proliferation to MSC (Fig. 1). Of note, THY+ FLS from these patients are localized around blood vessels within the synovium. In contrast, we found that in OA, THY1+ cells were localized to both the synovial lining and sublining layer but less prevalent around the blood vessels as previously described

(Mizoguchi et al., 2018). Finally, comparing FLS from OA patients with MSC not affected by inflammatory stimuli, we observed a different surface expression pattern of PDPN, THY1, and peptidases CD10 and CD26, a predominance of inflammatory proteins, and an increased proliferation rate in inflammation-exposed FLS from patients with OA (Fig. 2 and 3).

THY1+ FLS from patients with RA have recently been reported to adopt a glycolytic phenotype and demonstrate aberrantly increased cell growth in inflammatory niches (Mizoguchi et al., 2018). However, little is known about metabolic and functional alterations in FLS from patients with OA. Applying proteome analysis revealed an enrichment of GO-terms related to metabolic processes in FLS that are – unlike MSC – exposed to local inflammation, which can be attributed to pathogenic proliferative PDPN+THY1+ FLS due to the negligible number of PDPN+THY1- FLS in our isolation procedure (Fig. 4). As a novel finding, we noted that PDKs were highly expressed in pathogenic proliferative FLS compared to non-inflammatory MSC (Fig. 5). This was especially true for PDK3 – the isoenzyme with the highest activity and binding affinity for the PDH domain (Baker et al., 2000). In the OA synovium, FLS exhibited a prominent increase in PDK3 in PDPN+THY1+ cells of the lining layer compared to FLS from trauma patients without signs of chronic inflammation (Fig. 6). These PDK3+PDPN+THY1+ cells may (i) drive osteophyte development because THY1 was recently found to be essential for osteoblastogenesis (Paine et al., 2018) and (ii) increase cell survival and expansion associated with PDPN expression similar to many cancers (Krishnan et al., 2018). Based on these findings, we propose that the prominent PDPN expression and the PDK3-mediated metabolic shift of THY1+ FLS contribute to the pathogenesis of OA. However, it still remains unclear if the inflammatory milieu itself contributes to these changes.

All four known PDK isozymes (1-4) in human mitochondria are gatekeeping enzymes inhibiting the PDH complex (Linn et al., 1969). PDK1 and PDK3 have been shown to be involved in the hypoxia-induced metabolic shift towards glycolysis and better cell survival of highly proliferative cancer cells (Lu et al., 2008; Lu et al., 2011; Papandreou et al., 2006). Enhanced expression of PDKs correlated with phosphorylated PDHA1, a decrease in basal OCR, ATP-linked OCR, and coupling efficiency despite a higher spare respiratory capacity, a higher number of mitochondria/mitochondrial cristae, and

mitochondrial proteins as well as an increased glycolytic extracellular acidification (Fig. 5). Thus, they provide high amounts of ATP to the cellular energy pool and building blocks, as evidenced by high levels of steady-state ATP and the higher proliferation rate of these cells compared with non-inflammatory MSC. Since these findings persisted after isolation from the inflammatory environment and up to 4 cell passages *in vitro*, we assume a 'trained' metabolic adaptation of FLS to the inflammatory environment.

Despite previous reports on the transcriptional induction of glycolytic enzymes in FLS from patients with RA or OA (Bustamante et al., 2018; Garcia-Carbonell et al., 2016; Zhang et al., 2019; Zhao et al., 2016; Zou et al., 2017), we did not observe an induction of glycolytic enzyme expression in FLS using mass spectrometry (Supplementary Fig. 6). However, we observed an increase in glycolytic flux indicated by a high PER/OCR ratio (Fig. 5) and elevated lactate production (Fig. 7), although the carbon source of this effect is not extracellular glucose, can be assumed for fatty acid oxidation (FAO) but still needs to be elucidated (Fig. 7). In contrast, the expression of both glycolytic enzymes fueling the PPP and key enzymes of the PPP itself were increased in FLS compared to MSC. This fact supports the observation of higher cell proliferation in FLS than in MSC, underpinned by increased expression of cell cycle proteins, mediate cell transformation, and are involved in cancer-associated signaling pathways (Supplementary Fig. 7-10). It should be noted that the PPP flux is also up-regulated in proliferative transformed pannus-forming FLS from patients with RA (Ahn et al., 2016).

However, key regulatory enzymes of carbon and energy flux seem to vary in the variety of fibroblast niches, fibroblast subsets, and fibrotic diseases (Hewitson and Smith, 2021). For instance, activation of PDKs is assumed to be an essential metabolic switch to a fibrotic Warburg-like phenotype in renal and cardiac fibroblasts (Smith and Hewitson, 2020; Tian et al., 2020). Furthermore, PDKs have been proposed to be a sensitive marker of increased FAO (Pettersen et al., 2019). We also observed an association of PDK3 expression and a shift from glucose to fatty acids as a primary energy source as indicated by a higher expression of enzymes catalyzing FAO and fatty acid synthesis (FAS) (Supplementary Fig. 7), as well as the attenuation of DCA-mediated enhancement of OCR by ETO (Fig. 7). With regard to the contribution

of OA FLS to cartilage degradation, we identified a higher expression of enzymes facilitating cellular GAG degradation in FLS compared with MSC (Supplementary Fig. 11).

Finally, we confirmed that metabolic reprogramming of FLS by inhibiting PDKs and PDK-mediated PDHA1 phosphorylation using DCA shifts glycolytic metabolism to OXPHOS marked by decreasing lactate synthesis (Fig. 7) while reducing proliferation, proinflammatory cytokine, and chemokine secretion as well as PDPN expression without causing cell death (Fig. 8). We verified PDKs as potential pharmacological targets (Stacpoole, 2017). Given the selective overexpression of PDK3 in OA synovium and its restricted distribution in synovial tissue from trauma patients, PDKs represent the distinct mechanistic difference between healthy and diseased FLS. Therefore, they may serve as attractive selective targets for treating arthritis without affecting cells being in a homeostatic, oxidative state and, thus, might be safer than global inhibition of glycolysis (Hay, 2016).

Conclusion

This is the first study to identify PDK isoforms as contributors to metabolic changes in active proliferative synovial fibroblasts, namely PDPN+THY1+ FLS, in OA. Hypothesizing that synovitis-induced metabolic imbalances characterize chronic local inflammation exposed FLS in patients with OA, this study demonstrates that inhibition of PDKs – newly identified as overexpressed in OA – metabolically reprogrammed pathogenic proliferative THY1+ synovial fibroblasts as evidenced by a reduction of proliferation and cytokine-secretion. We newly identified PDPN+THY1- FLS in the synovial lining and PDPN+THY1+ FLS surrounding vessels in synovial specimens from trauma patients without signs of chronic inflammation. Moreover, we observed an increase in PDPN+THY1+ FLS in the lining layer as characteristic of OA synovium, with the majority of PDPN+ cells localized in both the synovial lining and sublining layer. Additional studies are required to understand how the expression of PDK in FLS subsets and their response to PDK inhibition varies in different joints and clinical contexts in OA, including the severity of disease activities, the prognosis of joint destruction, and response to therapies. Our studies also derive the well-founded presumption that PDKs represent a potential pharmacological target and novel

approach for combination therapy in OA and may serve as a target for pathogenic subsets of tissue cells in other human diseases.

Code Availability

The authors declare that *Pathview* is an open-source software package distributed under GPLv3. *Pathview* downloads and uses KEGG data.

Data availability

The mass spectrometry proteomics data have been deposited to the ProteomeXchange Consortium via the PRIDE (Perez-Riverol et al., 2019) partner repository with the dataset identifier PXD027215. Reviewer account details: reviewer_pxd027215@ebi.ac.uk (username), 5NW9PTFY (password).

Acknowledgements

The authors would like to thank Manuela Jakstadt for excellent technical assistance and the Tissue Harvesting Core Facility of the BIH Berlin for providing bone marrow. This research was supported by the Forschungsförderung der Charité–Universitätsmedizin Berlin and the ECRT Einstein Kickbox – Young Scientists Grant 2020. A.D. was gratefully supported by the Studienstiftung des deutschen Volkes and by the Joachim Herz Foundation (Add-on Fellowship 2020). T.G. was supported by the Deutsche Forschungsgemeinschaft (353142848).

Authors contributions

Alexandra Damerau: Conceptualization; data curation; formal analysis; funding acquisition, investigation; methodology; project administration, validation, visualization, writing-original draft; writing – review & editing. Marieluise Kirchner: Formal analysis; methodology; writing – review & editing. Moritz Pfeiffenberger: Methodology; writing – review & editing. Lisa Ehlers: Methodology; writing – review & editing. Duc Ha Do Nguyen: Methodology; writing – review & editing. Philipp Mertins: Methodology;

writing – review & editing. Benjamin Bartek: Resources; writing – review & editing. Tazio Maleitzke: Resources; writing – review & editing. Yannick Palmowski: Resources; writing – review & editing. Sebastian Hardt: Resources; writing – review & editing. Tobias Winkler: Resources; writing – review & editing. Frank Buttgereit: Data curation; funding acquisition; supervision; writing – review & editing. Timo Gaber: Conceptualization; data curation; project administration; supervision; validation, writing-original draft; writing – review & editing.

Financial Disclosure

This research did not receive any specific grant from funding agencies in the public, commercial, or not-for-profit sectors.

Competing interests

The authors have declared that no competing interests exist.

References

Abboud, G., Choi, S. C., Kanda, N., Zeumer-Spataro, L., Roopenian, D. C., Morel, L., 2018. Inhibition of Glycolysis Reduces Disease Severity in an Autoimmune Model of Rheumatoid Arthritis. Front Immunol. 9**,** 1973.

Abuwarwar, M. H., Knoblich, K., Fletcher, A. L., 2018. A pathogenic hierarchy for synovial fibroblasts in rheumatoid arthritis. Ann Transl Med. 6**,** S75.

Ahn, J. K., Kim, S., Hwang, J., Kim, J., Kim, K. H., Cha, H. S., 2016. GC/TOF-MS-based metabolomic profiling in cultured fibroblast-like synoviocytes from rheumatoid arthritis. Joint Bone Spine. 83**,** 707-713.

Ayala-Cuellar, A. P., Kang, J. H., Jeung, E. B., Choi, K. C., 2019. Roles of Mesenchymal Stem Cells in Tissue Regeneration and Immunomodulation. Biomol Ther (Seoul). 27**,** 25-33.

Baker, J. C., Yan, X., Peng, T., Kasten, S., Roche, T. E., 2000. Marked differences between two isoforms of human pyruvate dehydrogenase kinase. J Biol Chem. 275**,** 15773-81.

Berenbaum, F., 2013. Osteoarthritis as an inflammatory disease (osteoarthritis is not osteoarthrosis!). Osteoarthritis Cartilage. 21**,** 16-21.

Bhattaram, P., Chandrasekharan, U., 2017. The joint synovium: A critical determinant of articular cartilage fate in inflammatory joint diseases. Semin Cell Dev Biol. 62**,** 86-93.

Bustamante, M. F., Oliveira, P. G., Garcia-Carbonell, R., Croft, A. P., Smith, J. M., Serrano, R. L., Sanchez-Lopez, E., Liu, X., Kisseleva, T., Hay, N., Buckley, C. D., Firestein, G. S., Murphy, A. N., Miyamoto, S., Guma, M., 2018. Hexokinase 2 as a novel selective metabolic target for rheumatoid arthritis. Ann Rheum Dis. 77**,** 1636-1643.

Cai, S., Ming, B., Ye, C., Lin, S., Hu, P., Tang, J., Zheng, F., Dong, L., 2019. Similar Transition Processes in Synovial Fibroblasts from Rheumatoid Arthritis and Osteoarthritis: A Single-Cell Study. J Immunol Res. 2019**,** 4080735.

Chimenti, M. S., Triggianese, P., Conigliaro, P., Candi, E., Melino, G., Perricone, R., 2015. The interplay between inflammation and metabolism in rheumatoid arthritis. Cell Death Dis. 6**,** e1887.

Croft, A. P., Campos, J., Jansen, K., Turner, J. D., Marshall, J., Attar, M., Savary, L., Wehmeyer, C., Naylor, A. J., Kemble, S., Begum, J., Durholz, K., Perlman, H., Barone, F., McGettrick, H. M., Fearon, D. T., Wei, K., Raychaudhuri, S., Korsunsky, I., Brenner, M. B., Coles, M., Sansom, S. N., Filer, A., Buckley, C. D., 2019. Distinct fibroblast subsets drive inflammation and damage in arthritis. Nature. 570**,** 246-251.

765 Damerau, A., Pfeiffenberger, M., Weber, M. C., Burmester, G. R., Buttgereit, F., Gaber, T., Lang, A., 2020. A Human
766 Osteochondral Tissue Model Mimicking Cytokine-Induced Key Features of Arthritis In Vitro. Int J Mol Sci.
767 22.
768 de Oliveira, P. G., Farinon, M., Sanchez-Lopez, E., Miyamoto, S., Guma, M., 2019. Fibroblast-Like Synoviocytes
769 Glucose Metabolism as a Therapeutic Target in Rheumatoid Arthritis. Front Immunol. 10**,** 1743.
770 Denu, R. A., Nemcek, S., Bloom, D. D., Goodrich, A. D., Kim, J., Mosher, D. F., Hematti, P., 2016. Fibroblasts and
771 Mesenchymal Stromal/Stem Cells Are Phenotypically Indistinguishable. Acta Haematol. 136**,** 85-97.
772 Di Carlo, S. E., Peduto, L., 2018. The perivascular origin of pathological fibroblasts. J Clin Invest. 128**,** 54-63.
773 Ding, L., Vezzani, B., Khan, N., Su, J., Xu, L., Yan, G., Liu, Y., Li, R., Gaur, A., Diao, Z., Hu, Y., Yang, Z., Hardy,
774 W. R., James, A. W., Sun, H., Peault, B., 2020. CD10 expression identifies a subset of human perivascular
775 progenitor cells with high proliferation and calcification potentials. Stem Cells. 38**,** 261-275.
776 Dominici, M., Le Blanc, K., Mueller, I., Slaper-Cortenbach, I., Marini, F., Krause, D., Deans, R., Keating, A., Prockop,
777 D., Horwitz, E., 2006. Minimal criteria for defining multipotent mesenchymal stromal cells. The International
778 Society for Cellular Therapy position statement. Cytotherapy. 8**,** 315-7.
779 Ekwall, A. K., Eisler, T., Anderberg, C., Jin, C., Karlsson, N., Brisslert, M., Bokarewa, M. I., 2011. The tumour-
780 associated glycoprotein podoplanin is expressed in fibroblast-like synoviocytes of the hyperplastic synovial
781 lining layer in rheumatoid arthritis. Arthritis Res Ther. 13**,** R40.
782 Garcia-Carbonell, R., Divakaruni, A. S., Lodi, A., Vicente-Suarez, I., Saha, A., Cheroutre, H., Boss, G. R., Tiziani,
783 S., Murphy, A. N., Guma, M., 2016. Critical Role of Glucose Metabolism in Rheumatoid Arthritis Fibroblast-
784 like Synoviocytes. Arthritis Rheumatol. 68**,** 1614-26.
785 Hay, N., 2016. Reprogramming glucose metabolism in cancer: can it be exploited for cancer therapy? Nat Rev Cancer.
786 16**,** 635-49.
787 Hewitson, T. D., Smith, E. R., 2021. A Metabolic Reprogramming of Glycolysis and Glutamine Metabolism Is a
788 Requisite for Renal Fibrogenesis-Why and How? Front Physiol. 12**,** 645857.
789 Hunter, D. J., March, L., Chew, M., 2020. Osteoarthritis in 2020 and beyond: a Lancet Commission. Lancet. 396**,**
790 1711-1712.
791 Klemann, C., Wagner, L., Stephan, M., von Horsten, S., 2016. Cut to the chase: a review of CD26/dipeptidyl
792 peptidase-4's (DPP4) entanglement in the immune system. Clin Exp Immunol. 185**,** 1-21.

Krishnan, H., Rayes, J., Miyashita, T., Ishii, G., Retzbach, E. P., Sheehan, S. A., Takemoto, A., Chang, Y. W., Yoneda, K., Asai, J., Jensen, L., Chalise, L., Natsume, A., Goldberg, G. S., 2018. Podoplanin: An emerging cancer biomarker and therapeutic target. Cancer Sci. 109**,** 1292-1299.

Linn, T. C., Pettit, F. H., Reed, L. J., 1969. Alpha-keto acid dehydrogenase complexes. X. Regulation of the activity of the pyruvate dehydrogenase complex from beef kidney mitochondria by phosphorylation and dephosphorylation. Proc Natl Acad Sci U S A. 62**,** 234-41.

Lu, C. W., Lin, S. C., Chen, K. F., Lai, Y. Y., Tsai, S. J., 2008. Induction of pyruvate dehydrogenase kinase-3 by hypoxia-inducible factor-1 promotes metabolic switch and drug resistance. J Biol Chem. 283**,** 28106-14.

Lu, C. W., Lin, S. C., Chien, C. W., Lin, S. C., Lee, C. T., Lin, B. W., Lee, J. C., Tsai, S. J., 2011. Overexpression of pyruvate dehydrogenase kinase 3 increases drug resistance and early recurrence in colon cancer. Am J Pathol. 179**,** 1405-14.

Luo, W., Brouwer, C., 2013. Pathview: an R/Bioconductor package for pathway-based data integration and visualization. Bioinformatics. 29**,** 1830-1.

Luo, W., Pant, G., Bhavnasi, Y. K., Blanchard, S. G., Jr., Brouwer, C., 2017. Pathview Web: user friendly pathway visualization and data integration. Nucleic Acids Res. 45**,** W501-W508.

Masoumi, M., Mehrabzadeh, M., Mahmoudzehi, S., Mousavi, M. J., Jamalzehi, S., Sahebkar, A., Karami, J., 2020. Role of glucose metabolism in aggressive phenotype of fibroblast-like synoviocytes: Latest evidence and therapeutic approaches in rheumatoid arthritis. Int Immunopharmacol. 89**,** 107064.

Mathiessen, A., Conaghan, P. G., 2017. Synovitis in osteoarthritis: current understanding with therapeutic implications. Arthritis Res Ther. 19**,** 18.

McGarry, T., Fearon, U., 2019. Cell metabolism as a potentially targetable pathway in RA. Nat Rev Rheumatol. 15**,** 70-72.

Mizoguchi, F., Slowikowski, K., Wei, K., Marshall, J. L., Rao, D. A., Chang, S. K., Nguyen, H. N., Noss, E. H., Turner, J. D., Earp, B. E., Blazar, P. E., Wright, J., Simmons, B. P., Donlin, L. T., Kalliolias, G. D., Goodman, S. M., Bykerk, V. P., Ivashkiv, L. B., Lederer, J. A., Hacohen, N., Nigrovic, P. A., Filer, A., Buckley, C. D., Raychaudhuri, S., Brenner, M. B., 2018. Functionally distinct disease-associated fibroblast subsets in rheumatoid arthritis. Nat Commun. 9**,** 789.

Muller-Ladner, U., Ospelt, C., Gay, S., Distler, O., Pap, T., 2007. Cells of the synovium in rheumatoid arthritis. Synovial fibroblasts. Arthritis Res Ther. 9**,** 223.

Nacarelli, T., Azar, A., Altinok, O., Orynbayeva, Z., Sell, C., 2018. Rapamycin increases oxidative metabolism and enhances metabolic flexibility in human cardiac fibroblasts. Geroscience.

Najar, M., Melki, R., Khalife, F., Lagneaux, L., Bouhtit, F., Moussa Agha, D., Fahmi, H., Lewalle, P., Fayyad-Kazan, M., Merimi, M., 2021. Therapeutic Mesenchymal Stem/Stromal Cells: Value, Challenges and Optimization. Front Cell Dev Biol. 9**,** 716853.

Nemoto, E., Sugawara, S., Takada, H., Shoji, S., Horiuch, H., 1999. Increase of CD26/dipeptidyl peptidase IV expression on human gingival fibroblasts upon stimulation with cytokines and bacterial components. Infect Immun. 67**,** 6225-33.

O'Neill, T. W., Felson, D. T., 2018. Mechanisms of Osteoarthritis (OA) Pain. Curr Osteoporos Rep. 16**,** 611-616.

Ospelt, C., Mertens, J. C., Jungel, A., Brentano, F., Maciejewska-Rodriguez, H., Huber, L. C., Hemmatazad, H., Wuest, T., Knuth, A., Gay, R. E., Michel, B. A., Gay, S., Renner, C., Bauer, S., 2010. Inhibition of fibroblast activation protein and dipeptidylpeptidase 4 increases cartilage invasion by rheumatoid arthritis synovial fibroblasts. Arthritis Rheum. 62**,** 1224-35.

Paine, A., Woeller, C. F., Zhang, H., de la Luz Garcia-Hernandez, M., Huertas, N., Xing, L., Phipps, R. P., Ritchlin, C. T., 2018. Thy1 is a positive regulator of osteoblast differentiation and modulates bone homeostasis in obese mice. FASEB J. 32**,** 3174-3183.

Papandreou, I., Cairns, R. A., Fontana, L., Lim, A. L., Denko, N. C., 2006. HIF-1 mediates adaptation to hypoxia by actively downregulating mitochondrial oxygen consumption. Cell Metab. 3**,** 187-97.

Pendleton, A., Arden, N., Dougados, M., Doherty, M., Bannwarth, B., Bijlsma, J. W., Cluzeau, F., Cooper, C., Dieppe, P. A., Gunther, K. P., Hauselmann, H. J., Herrero-Beaumont, G., Kaklamanis, P. M., Leeb, B., Lequesne, M., Lohmander, S., Mazieres, B., Mola, E. M., Pavelka, K., Serni, U., Swoboda, B., Verbruggen, A. A., Weseloh, G., Zimmermann-Gorska, I., 2000. EULAR recommendations for the management of knee osteoarthritis: report of a task force of the Standing Committee for International Clinical Studies Including Therapeutic Trials (ESCISIT). Ann Rheum Dis. 59**,** 936-44.

Perez-Riverol, Y., Csordas, A., Bai, J., Bernal-Llinares, M., Hewapathirana, S., Kundu, D. J., Inuganti, A., Griss, J., Mayer, G., Eisenacher, M., Perez, E., Uszkoreit, J., Pfeuffer, J., Sachsenberg, T., Yilmaz, S., Tiwary, S., Cox,

J., Audain, E., Walzer, M., Jarnuczak, A. F., Ternent, T., Brazma, A., Vizcaino, J. A., 2019. The PRIDE database and related tools and resources in 2019: improving support for quantification data. Nucleic Acids Res. 47**,** D442-D450.

Pettersen, I. K. N., Tusubira, D., Ashrafi, H., Dyrstad, S. E., Hansen, L., Liu, X. Z., Nilsson, L. I. H., Lovsletten, N. G., Berge, K., Wergedahl, H., Bjorndal, B., Fluge, O., Bruland, O., Rustan, A. C., Halberg, N., Rosland, G. V., Berge, R. K., Tronstad, K. J., 2019. Upregulated PDK4 expression is a sensitive marker of increased fatty acid oxidation. Mitochondrion. 49**,** 97-110.

Pfeiffenberger, M., Hoff, P., Thone-Reineke, C., Buttgereit, F., Lang, A., Gaber, T., 2020. The in vitro human fracture hematoma model - a tool for preclinical drug testing. ALTEX. 37**,** 561-578.

Quintanilla, M., Montero-Montero, L., Renart, J., Martin-Villar, E., 2019. Podoplanin in Inflammation and Cancer. Int J Mol Sci. 20.

Rappsilber, J., Ishihama, Y., Mann, M., 2003. Stop and go extraction tips for matrix-assisted laser desorption/ionization, nanoelectrospray, and LC/MS sample pretreatment in proteomics. Anal Chem. 75**,** 663-70.

Smith, E. R., Hewitson, T. D., 2020. TGF-beta1 is a regulator of the pyruvate dehydrogenase complex in fibroblasts. Sci Rep. 10**,** 17914.

Smith, R. L., Soeters, M. R., Wust, R. C. I., Houtkooper, R. H., 2018. Metabolic Flexibility as an Adaptation to Energy Resources and Requirements in Health and Disease. Endocr Rev. 39**,** 489-517.

Smolen, J. S., Landewe, R. B. M., Bijlsma, J. W. J., Burmester, G. R., Dougados, M., Kerschbaumer, A., McInnes, I. B., Sepriano, A., van Vollenhoven, R. F., de Wit, M., Aletaha, D., Aringer, M., Askling, J., Balsa, A., Boers, M., den Broeder, A. A., Buch, M. H., Buttgereit, F., Caporali, R., Cardiel, M. H., De Cock, D., Codreanu, C., Cutolo, M., Edwards, C. J., van Eijk-Hustings, Y., Emery, P., Finckh, A., Gossec, L., Gottenberg, J. E., Hetland, M. L., Huizinga, T. W. J., Koloumas, M., Li, Z., Mariette, X., Muller-Ladner, U., Mysler, E. F., da Silva, J. A. P., Poor, G., Pope, J. E., Rubbert-Roth, A., Ruyssen-Witrand, A., Saag, K. G., Strangfeld, A., Takeuchi, T., Voshaar, M., Westhovens, R., van der Heijde, D., 2020. EULAR recommendations for the management of rheumatoid arthritis with synthetic and biological disease-modifying antirheumatic drugs: 2019 update. Ann Rheum Dis. 79**,** 685-699.

Soare, A., Gyorfi, H. A., Matei, A. E., Dees, C., Rauber, S., Wohlfahrt, T., Chen, C. W., Ludolph, I., Horch, R. E., Bauerle, T., von Horsten, S., Mihai, C., Distler, O., Ramming, A., Schett, G., Distler, J. H. W., 2020. Dipeptidylpeptidase 4 as a Marker of Activated Fibroblasts and a Potential Target for the Treatment of Fibrosis in Systemic Sclerosis. Arthritis Rheumatol. 72**,** 137-149.

Sokolove, J., Lepus, C. M., 2013. Role of inflammation in the pathogenesis of osteoarthritis: latest findings and interpretations. Ther Adv Musculoskelet Dis. 5**,** 77-94.

Solan, N. J., Ward, P. E., Sanders, S. P., Towns, M. C., Bathon, J. M., 1998. Soluble recombinant neutral endopeptidase (CD10) as a potential antiinflammatory agent. Inflammation. 22**,** 107-21.

Stacpoole, P. W., 2017. Therapeutic Targeting of the Pyruvate Dehydrogenase Complex/Pyruvate Dehydrogenase Kinase (PDC/PDK) Axis in Cancer. J Natl Cancer Inst. 109.

Supek, F., Bosnjak, M., Skunca, N., Smuc, T., 2011. REVIGO summarizes and visualizes long lists of gene ontology terms. PLoS One. 6**,** e21800.

Tian, L., Wu, D., Dasgupta, A., Chen, K. H., Mewburn, J., Potus, F., Lima, P. D. A., Hong, Z., Zhao, Y. Y., Hindmarch, C. C. T., Kutty, S., Provencher, S., Bonnet, S., Sutendra, G., Archer, S. L., 2020. Epigenetic Metabolic Reprogramming of Right Ventricular Fibroblasts in Pulmonary Arterial Hypertension: A Pyruvate Dehydrogenase Kinase-Dependent Shift in Mitochondrial Metabolism Promotes Right Ventricular Fibrosis. Circ Res. 126**,** 1723-1745.

Tyanova, S., Temu, T., Cox, J., 2016. The MaxQuant computational platform for mass spectrometry-based shotgun proteomics. Nat Protoc. 11**,** 2301-2319.

Ugurlu, B., Karaoz, E., 2020. Comparison of similar cells: Mesenchymal stromal cells and fibroblasts. Acta Histochem. 122**,** 151634.

Ullah, I., Subbarao, R. B., Rho, G. J., 2015. Human mesenchymal stem cells - current trends and future prospective. Biosci Rep. 35.

Vazquez, A., Liu, J., Zhou, Y., Oltvai, Z. N., 2010. Catabolic efficiency of aerobic glycolysis: the Warburg effect revisited. BMC Syst Biol. 4**,** 58.

Wang, X., Hunter, D. J., Jin, X., Ding, C., 2018. The importance of synovial inflammation in osteoarthritis: current evidence from imaging assessments and clinical trials. Osteoarthritis Cartilage. 26**,** 165-174.

Wang, X., Shen, X., Yan, Y., Li, H., 2021. Pyruvate dehydrogenase kinases (PDKs): an overview toward clinical applications. Biosci Rep. 41.

Ward, L. S. C., Sheriff, L., Marshall, J. L., Manning, J. E., Brill, A., Nash, G. B., McGettrick, H. M., 2019. Podoplanin regulates the migration of mesenchymal stromal cells and their interaction with platelets. J Cell Sci. 132.

Woolbright, B. L., Rajendran, G., Harris, R. A., Taylor, J. A., 3rd, 2019. Metabolic Flexibility in Cancer: Targeting the Pyruvate Dehydrogenase Kinase:Pyruvate Dehydrogenase Axis. Mol Cancer Ther. 18**,** 1673-1681.

Zakhari, S., 2006. Overview: how is alcohol metabolized by the body? Alcohol Res Health. 29**,** 245-54.

Zhang, F., Wei, K., Slowikowski, K., Fonseka, C. Y., Rao, D. A., Kelly, S., Goodman, S. M., Tabechian, D., Hughes, L. B., Salomon-Escoto, K., Watts, G. F. M., Jonsson, A. H., Rangel-Moreno, J., Meednu, N., Rozo, C., Apruzzese, W., Eisenhaure, T. M., Lieb, D. J., Boyle, D. L., Mandelin, A. M., 2nd, Accelerating Medicines Partnership Rheumatoid, A., Systemic Lupus Erythematosus, C., Boyce, B. F., DiCarlo, E., Gravallese, E. M., Gregersen, P. K., Moreland, L., Firestein, G. S., Hacohen, N., Nusbaum, C., Lederer, J. A., Perlman, H., Pitzalis, C., Filer, A., Holers, V. M., Bykerk, V. P., Donlin, L. T., Anolik, J. H., Brenner, M. B., Raychaudhuri, S., 2019. Defining inflammatory cell states in rheumatoid arthritis joint synovial tissues by integrating single-cell transcriptomics and mass cytometry. Nat Immunol. 20**,** 928-942.

Zhao, Y., Yan, X., Li, X., Zheng, Y., Li, S., Chang, X., 2016. PGK1, a glucose metabolism enzyme, may play an important role in rheumatoid arthritis. Inflamm Res. 65**,** 815-25.

Zou, Y., Zeng, S., Huang, M., Qiu, Q., Xiao, Y., Shi, M., Zhan, Z., Liang, L., Yang, X., Xu, H., 2017. Inhibition of 6-phosphofructo-2-kinase suppresses fibroblast-like synoviocytes-mediated synovial inflammation and joint destruction in rheumatoid arthritis. Br J Pharmacol. 174**,** 893-908.

Supplementary Figures

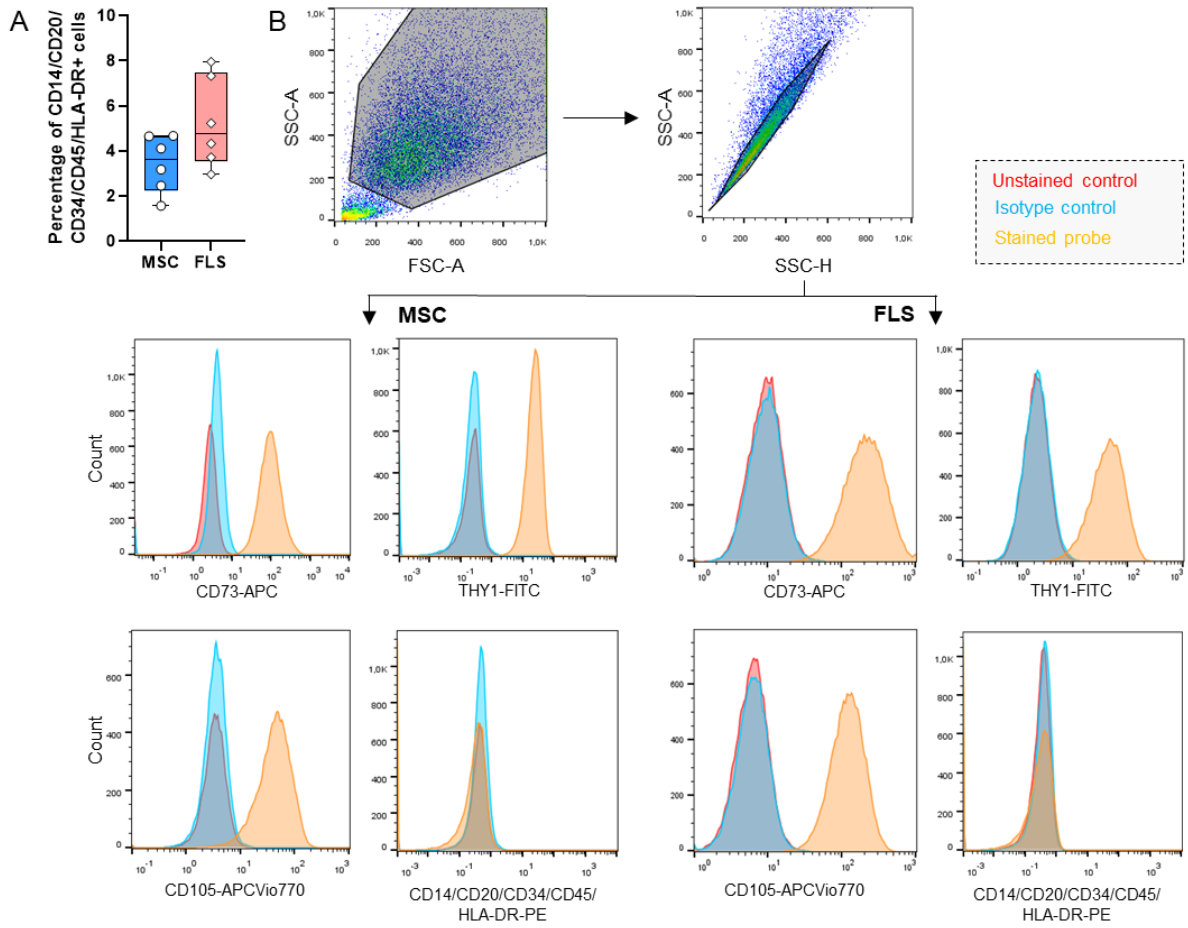

Supplementary Fig. 1. Flow cytometric characterization of FLS from patients with OA and MSC. (*A*) Surface expression of CD14, CD20, CD34, CD45, HLA-DR was evaluated using flow cytometry (n=6). Data are shown as box plots (center line, median; box limits, upper and lower quartiles; whiskers, maximum and minimum values; all data points). Statistics: Two-tailed Mann-Whitney U test. (*B*) Gating strategy. Cells were gated using a forward-scatter and side-scatter plot. Doublets were excluded according the side-scatter area and height pattern. The fractions were analyzed by flow cytometry using the MACSQuant® Analyzer 10. Each histogram was overlaid with the corresponding isotype control to identify positvely stained cells.

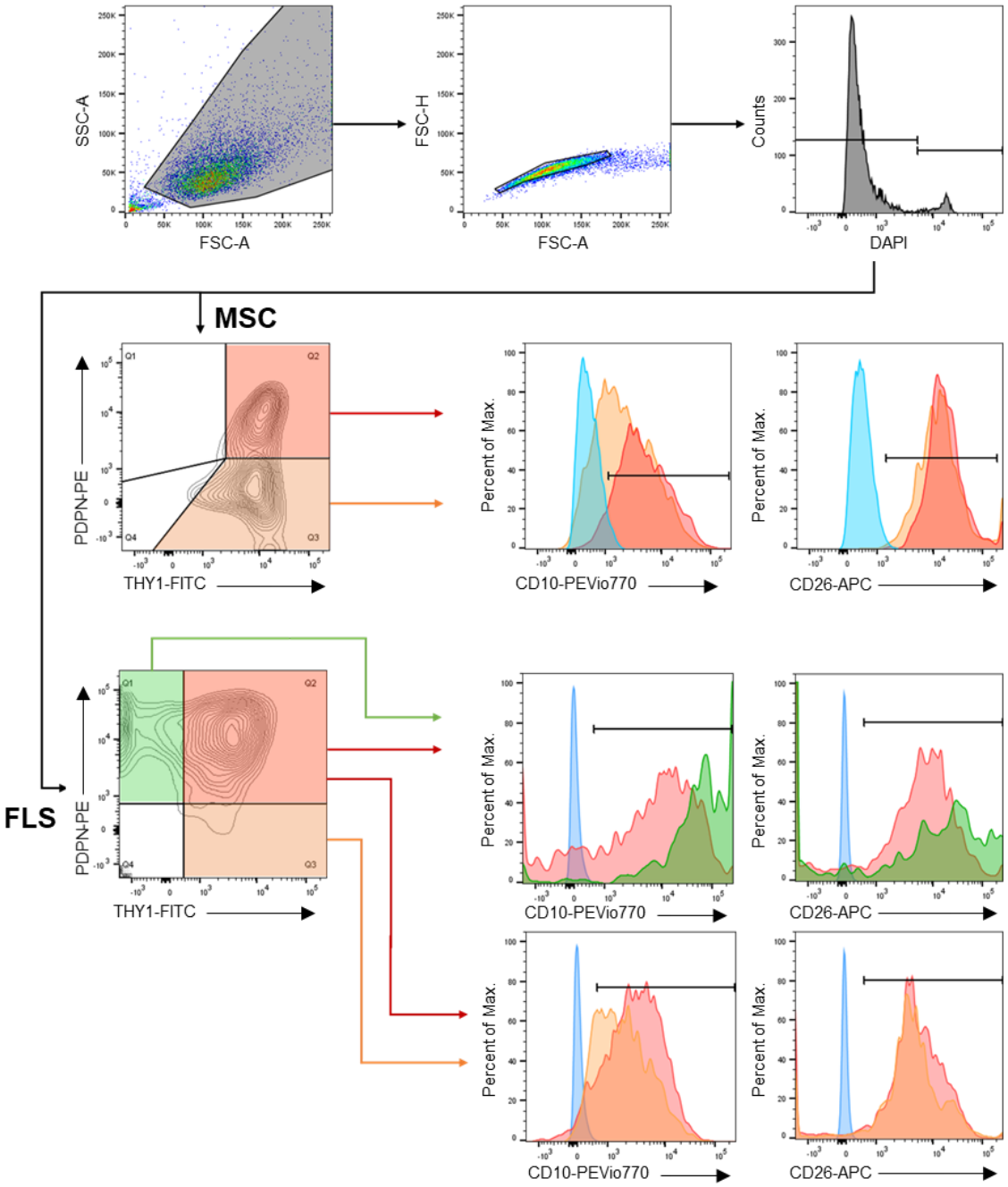

Supplementary Fig. 2. Gating strategy. Cells were gated using a forward-scatter and side-scatter plot. Doublets were excluded according the forward-scatter area and height pattern and DAPI was used to exclude dead cells. MSC and FLS were subdivided into PDPN+THY1+, PDPN+THY1-, and PDPN-THY1+ cell subsets. These cell subsets were characterized by the expression of CD10 and CD26, respectively. Histogram was overlaid with the corresponding unstained control (blue) to identify positvely stained cells.

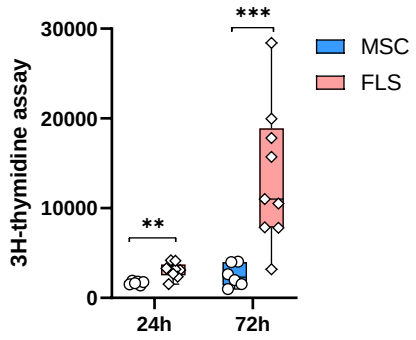

Supplementary Fig. 3. 3H-thymidine assay. 3H-thymidine assay was conducted after 24 h and 72 h to analyze the proliferation rate of synovial fibroblasts (FLS, n=9) and mesenchymal stromal cells (MSC, n=6) from patients with OA. Data are shown as box plots (center line, median; box limits, upper and lower quartiles; whiskers, maximum and minimum values; all data points). Statistics: Two-tailed Mann-Whitney U test; p-values are indicated in the graphs with **p<0.01, ***p<0.001.

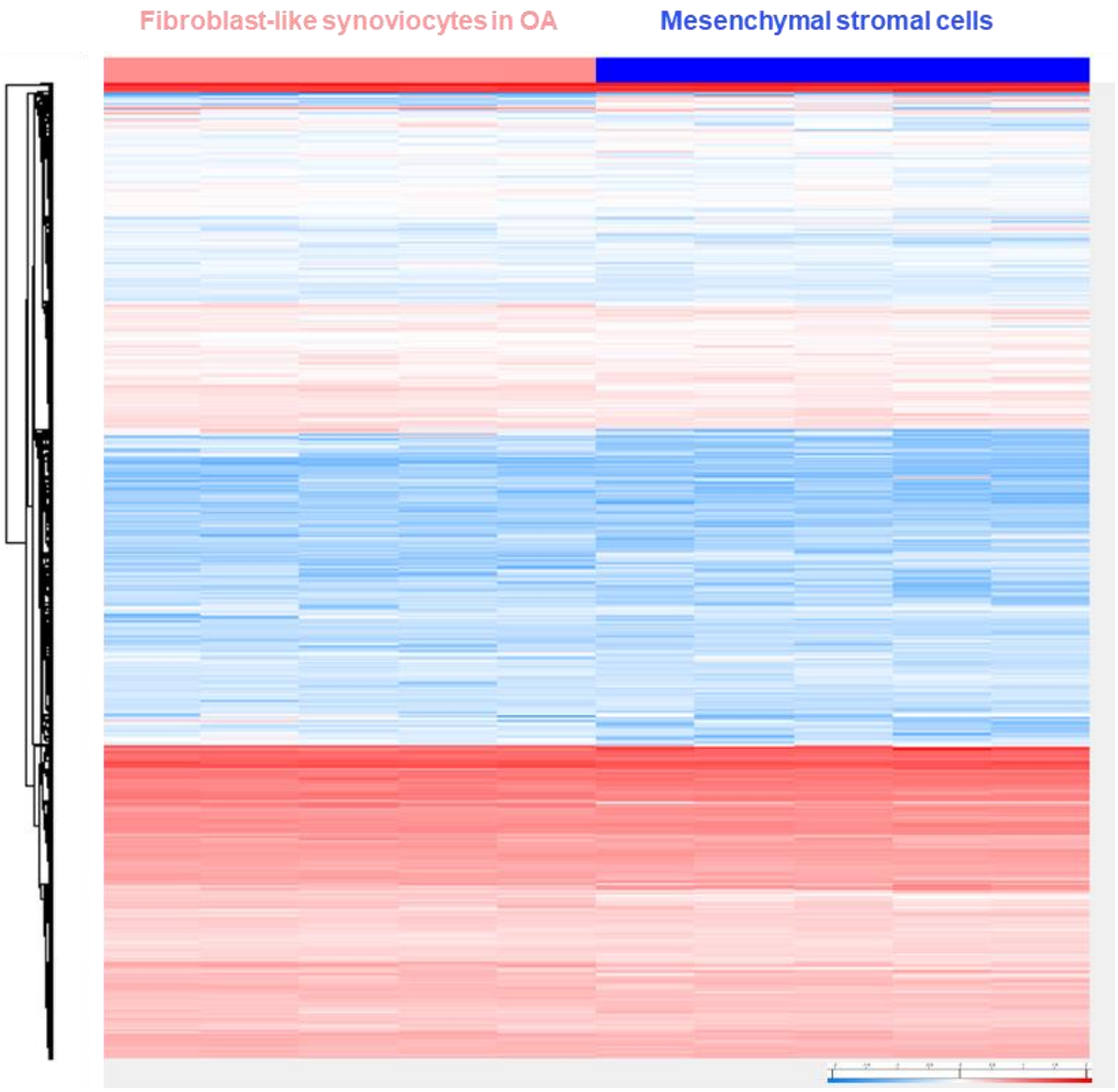

Supplementary Fig. 4. Heatmap of proteome data comparing synovial fibroblast and mesenchymal stromal cells from patients with OA (n=5).

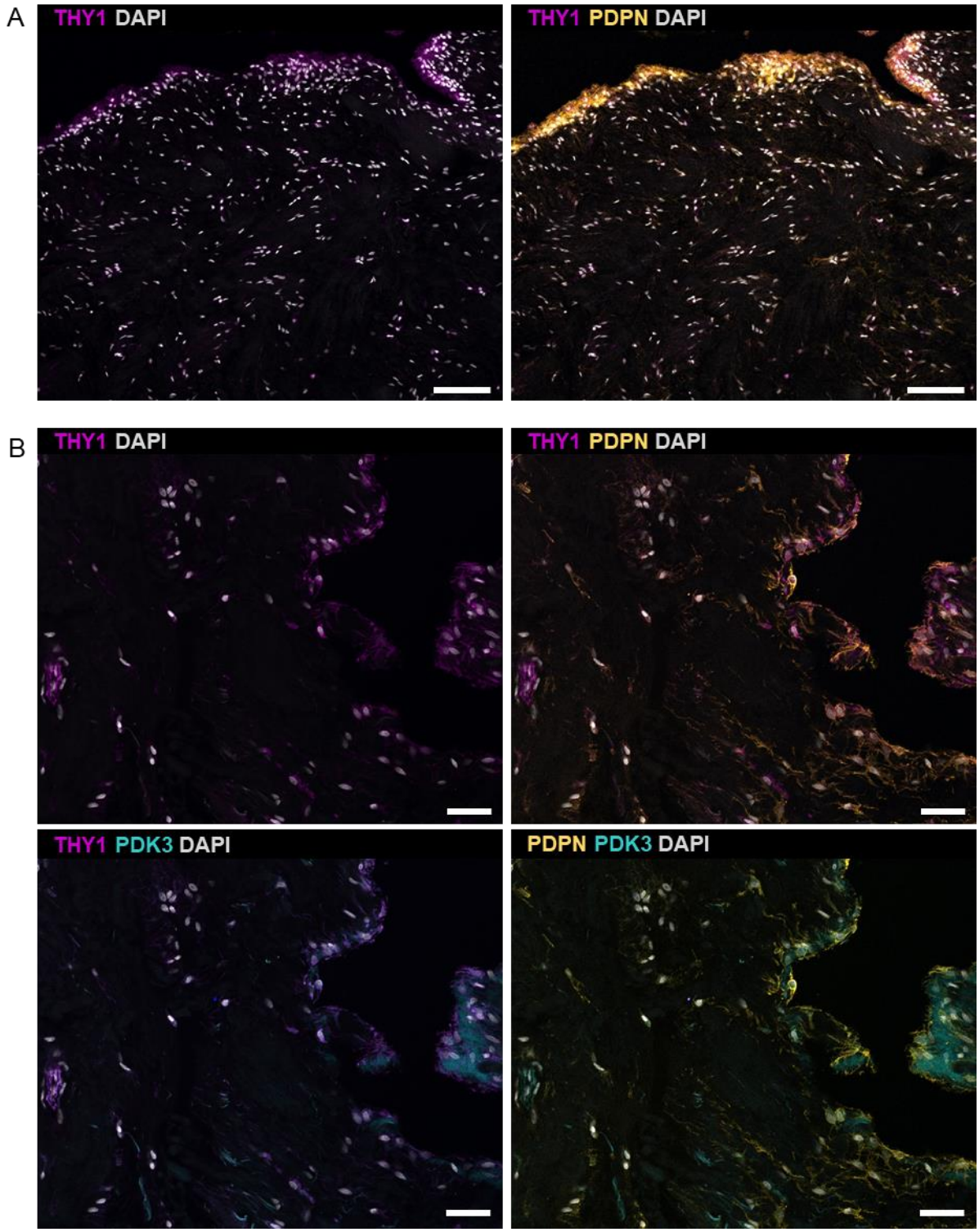

Supplementary Fig. 5. Confocal microscopy of OA synovium. (*A*, *B*) Proportions of fibroblast subsets and cellular localization and spatial distribution of PDK3 in synovial tissue sections from patients with OA (exemplary images of two donors). DAPI: gray, THY1: magenta, PDPN: yellow, PDK3: cyan. Scale bars show 50 µm.

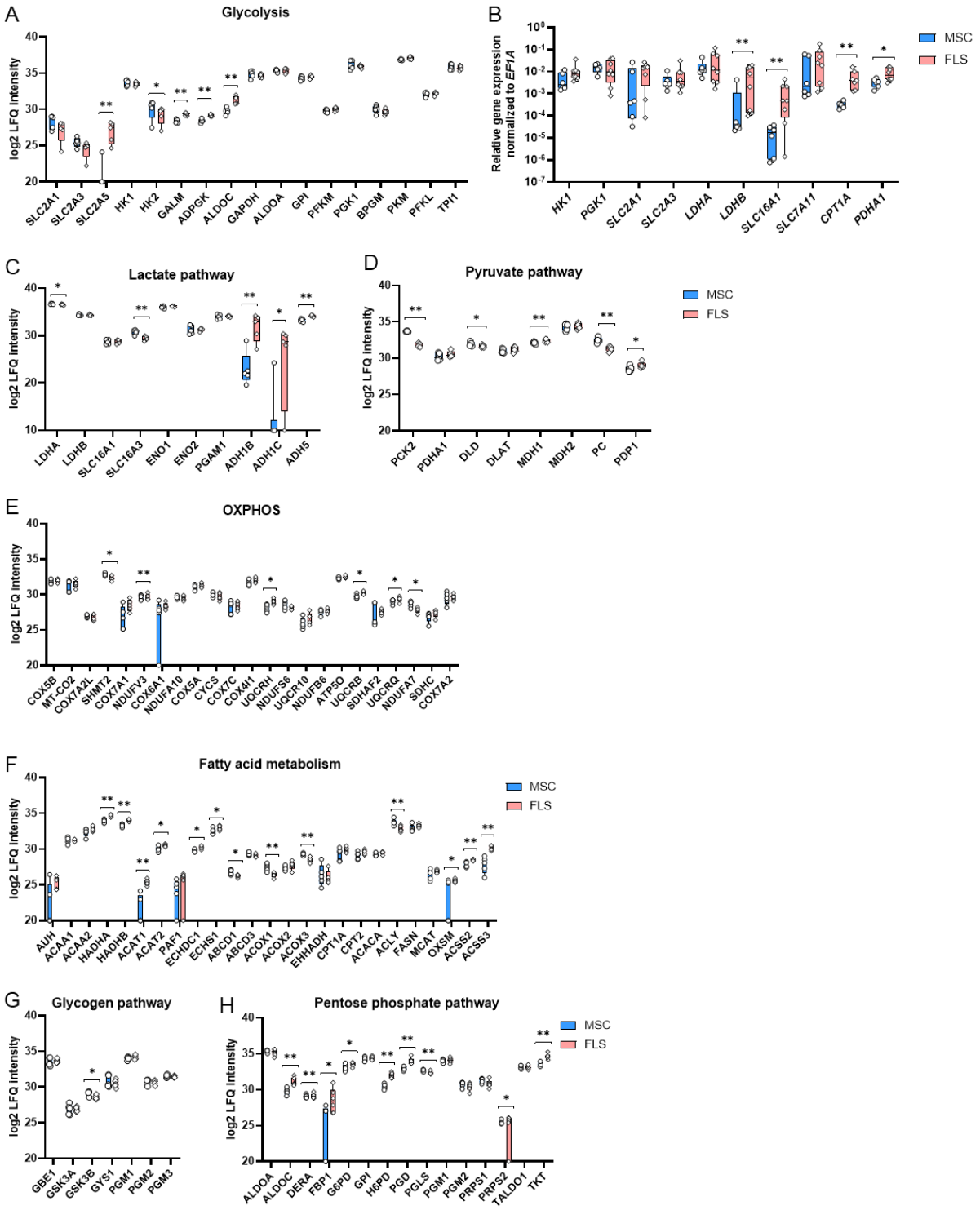

Supplementary Fig. 6. Metabolic pathway analysis correlates with the highly expressed pyruvate dehydrogenase kinase 3 in synovial fibroblasts in osteoarthritis. *A, C-H* Protein abundance of individual proteins belonging to indicated pathways (n=5). Shown are log2 transformed LFQ intensity values. (*A*) Glycolysis-related proteins. (*B*) Gene expression of selected pathway-relevant genes was normalized to the housekeeper gene *EF1A* (MSC: n=6; FLS: n=8). (*C*) Lactate pathway, (*D*) Pyruvate pathway, (*E*) Oxidative phosphorylation, (*F*) Fatty acid metabolism, (*G*) Glycogen pathway, Pentose phosphate pathway (PPP). Data shown as box plots (centre line, median; box limits, upper and lower quartiles; whiskers, maximum and minimum values; all data points). Statistics: Two-tailed Mann-Whitney U test; p-values are indicated in the graphs with *p<0.05, **p<0.01.

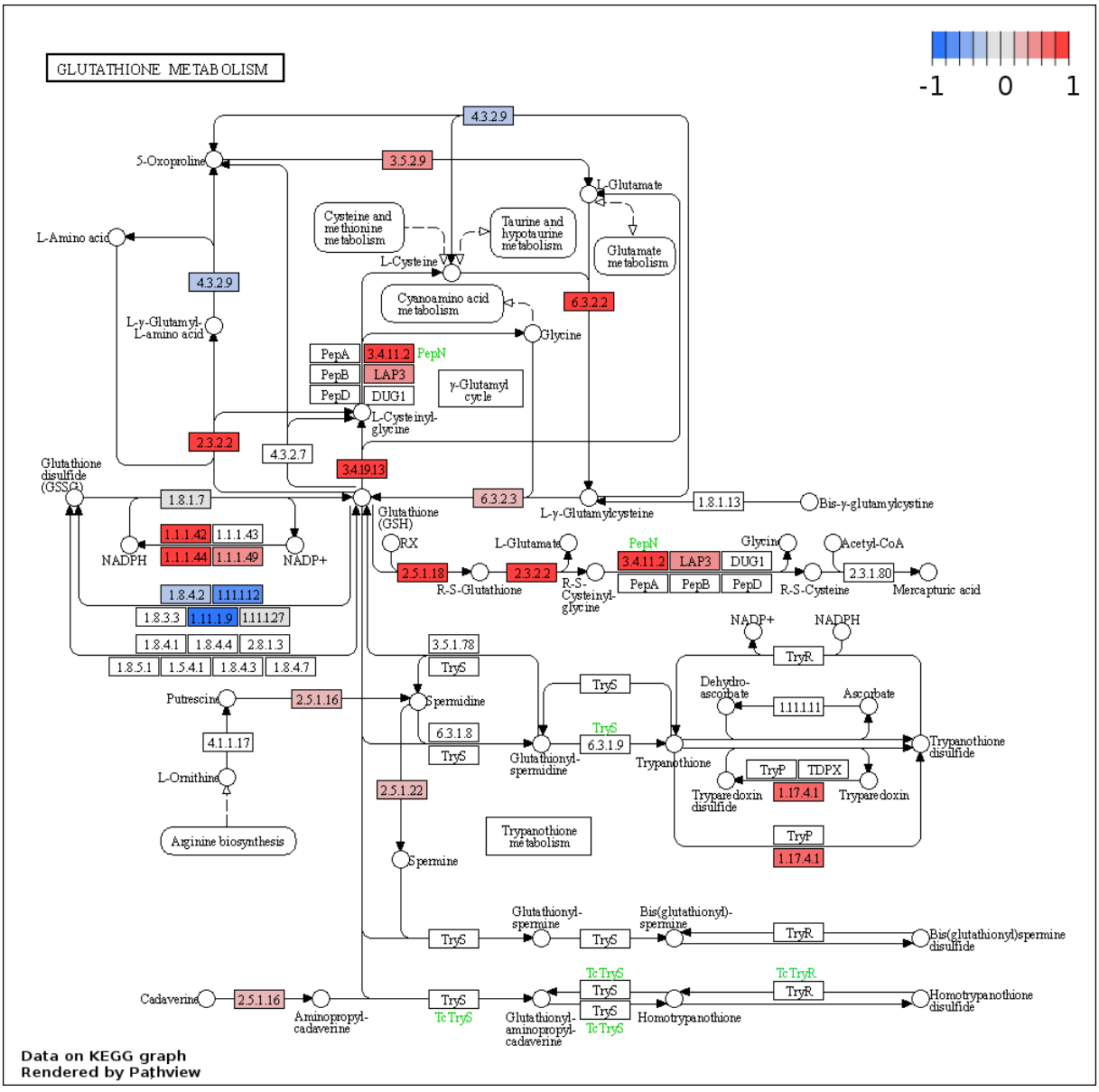

Supplementary Fig. 7. Glutathione metabolism. Overview of proteomic data on KEGG pathway maps using Pathview comparing synovial fibroblasts (FLS; n=5) and non-inflammatory mesenchymal stromal cells (MSCs, (n=5) from patients with osteoarthritis. Legend: Red (+1) = highly expressed in FLS; blue (-1) = highly expressed in MSCs.

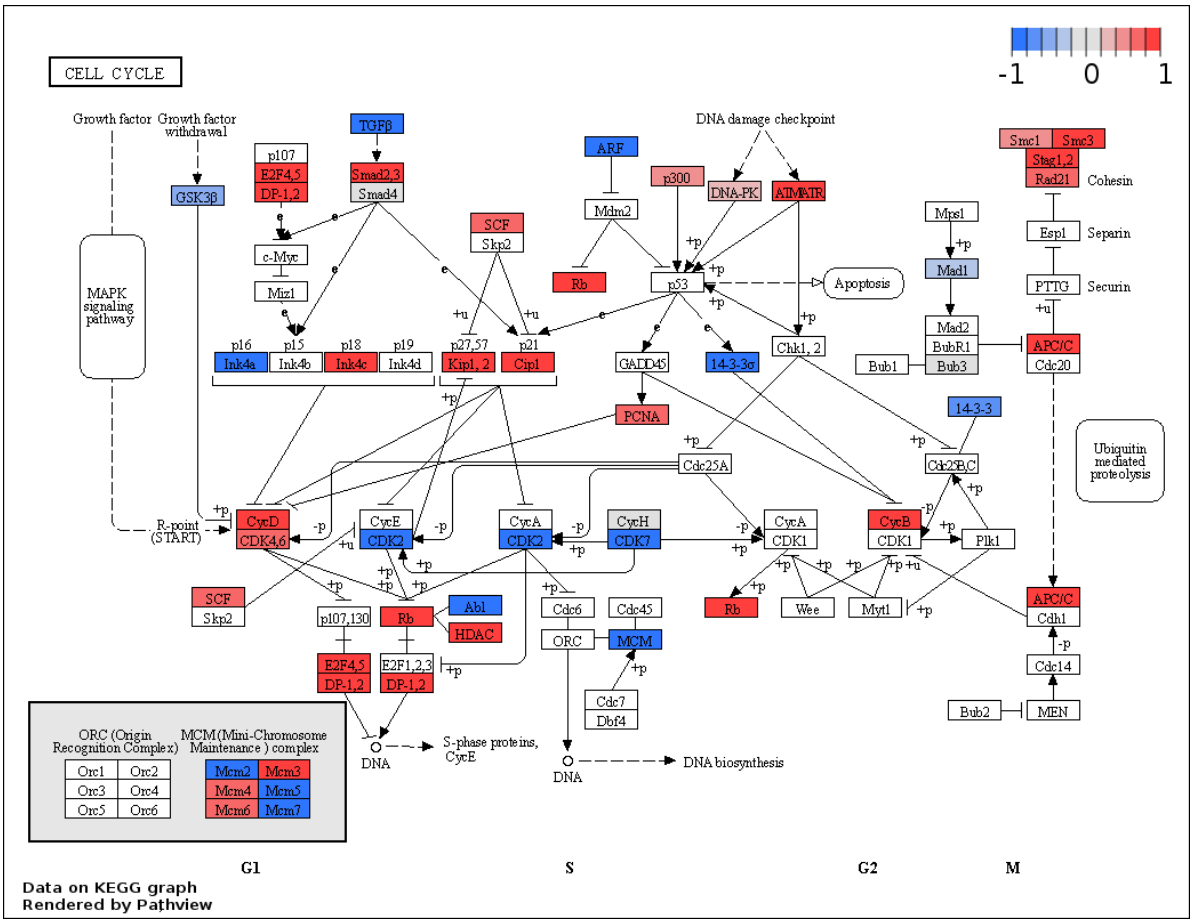

Supplementary Fig. 8. Cell cycle. Overview of proteomic data on KEGG pathway maps using Pathview comparing synovial fibroblasts (FLS; n=5) and non-inflammatory mesenchymal stromal cells (MSCs, (n=5) from patients with osteoarthritis. Legend: Red (+1) = highly expressed in FLS; blue (-1) = highly expressed in MSCs.

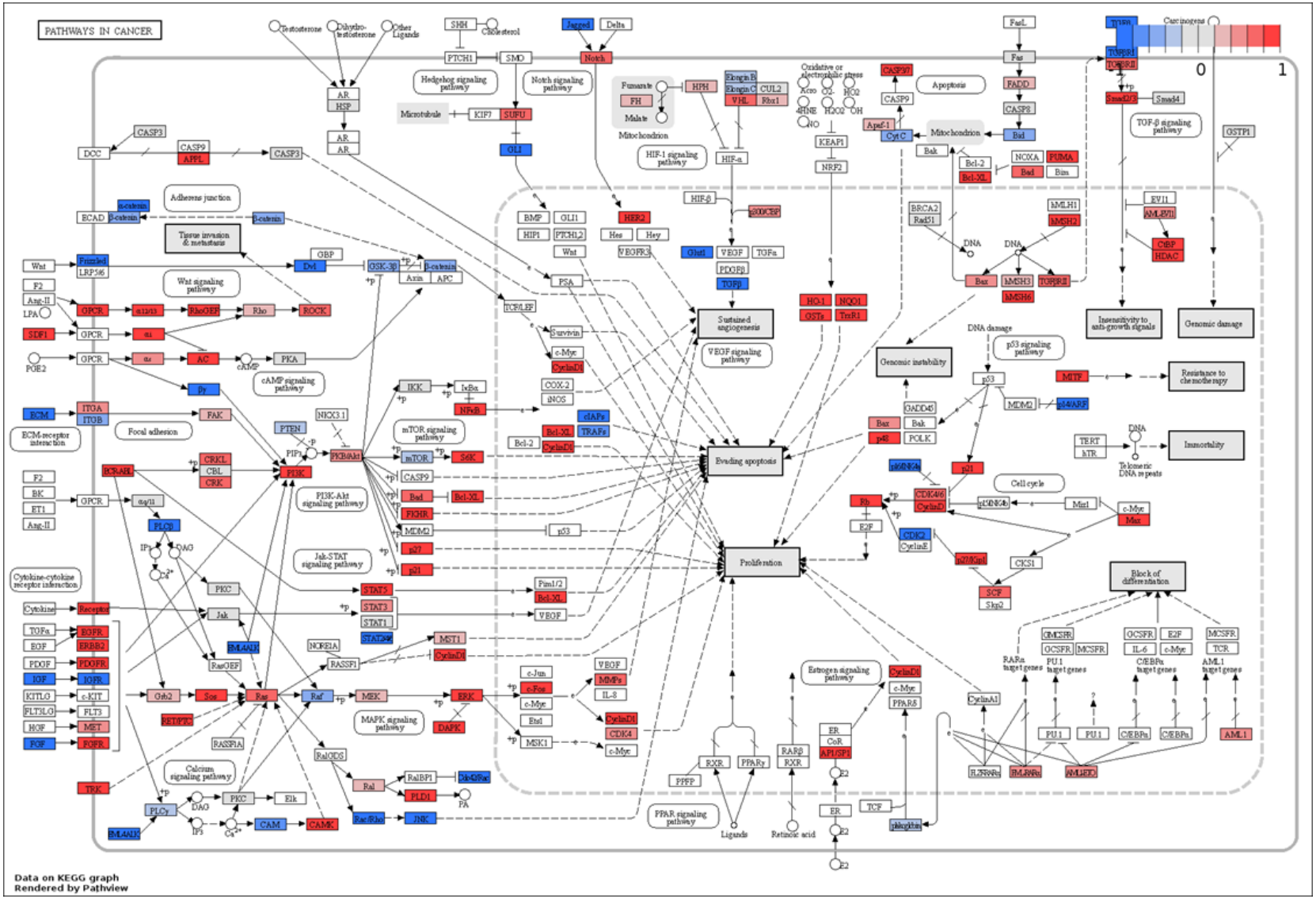

Supplementary Fig. 9. Pathways in cancer. Overview of proteomic data on KEGG pathway maps using Pathview comparing synovial fibroblasts (FLS; n=5) and non-inflammatory mesenchymal stromal cells (MSCs, (n=5) from patients with osteoarthritis. Legend: Red (+1) = highly expressed in FLS; blue (-1) = highly expressed in MSCs.

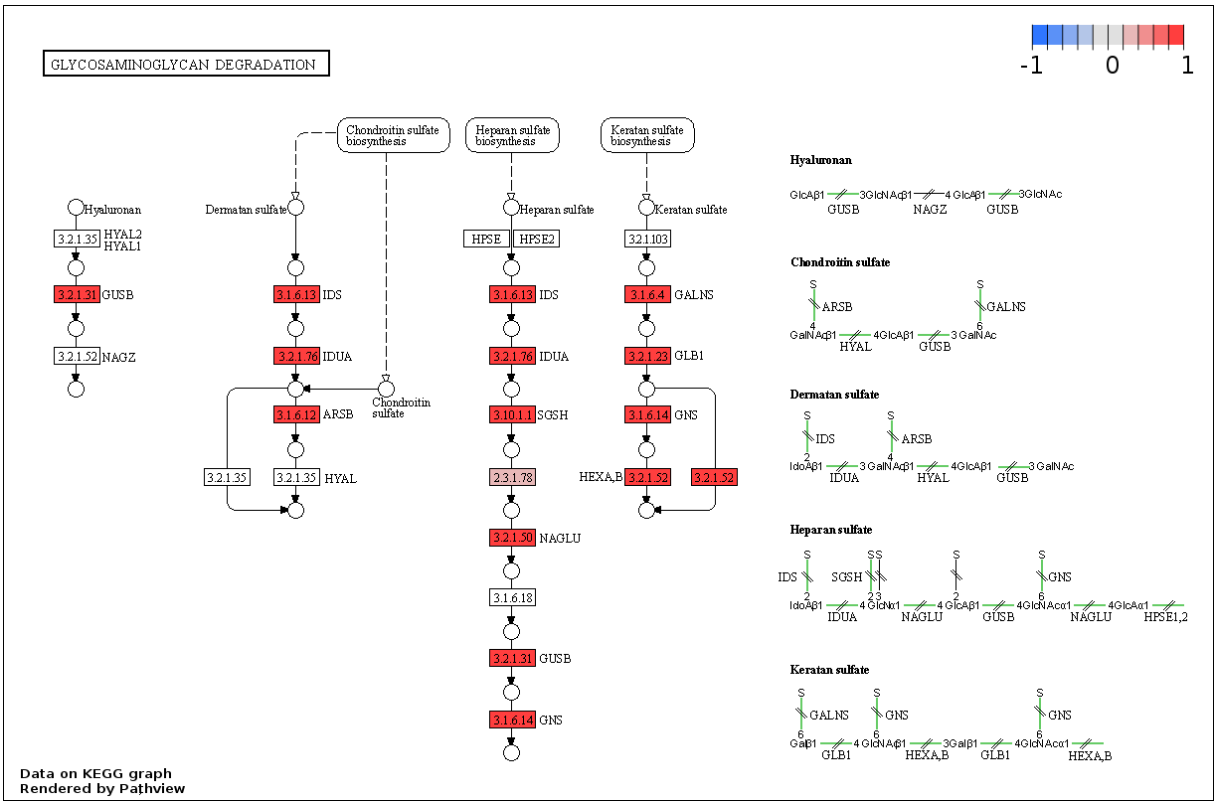

Supplementary Fig. 10. Glycosaminoglycan degradation. Overview of proteomic data on KEGG pathway maps using Pathview comparing synovial fibroblasts (FLS; n=5) and non-inflammatory mesenchymal stromal cells (MSCs, (n=5) from patients with osteoarthritis. Legend: Red (+1) = highly expressed in FLS; blue (-1) = highly expressed in MSCs.

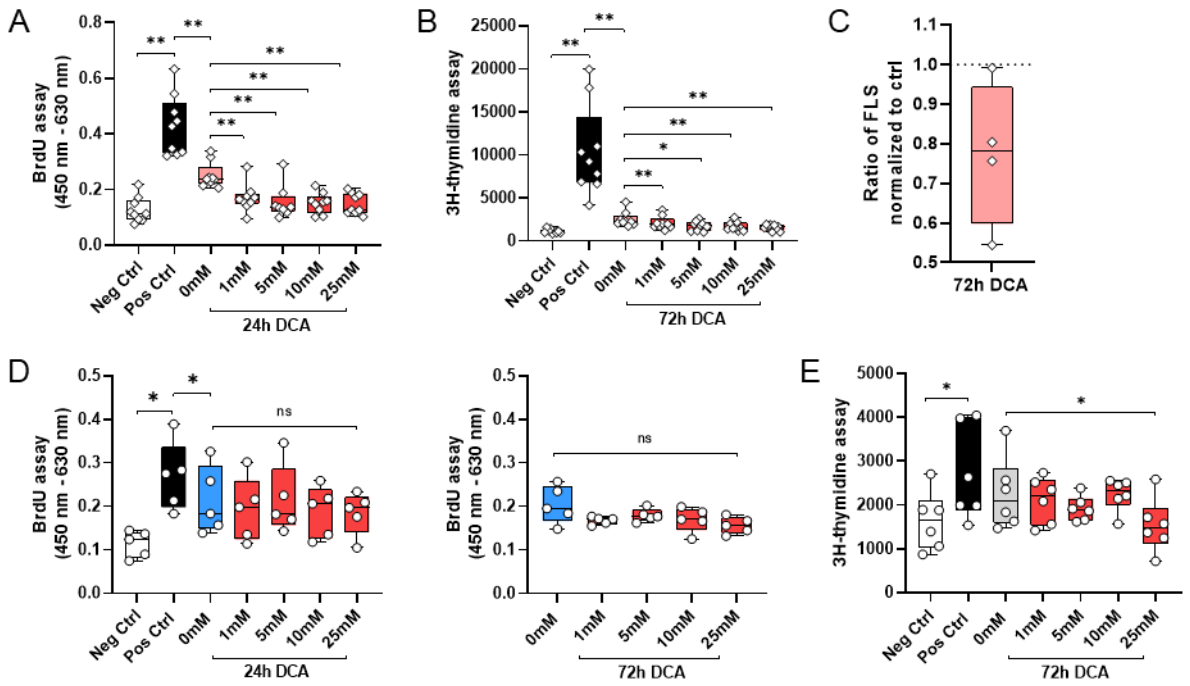

Supplementary Fig. 11. Effects of dichloroacetat (DCA) on cell proliferation. (*A*) BrdU assay and (*B*) 3H-thymidine assay were conducted to analyze the proliferation rate of synovial fibroblasts in osteoarthritis (n=10). (*C*) Ratio of synovial fibroblasts (FLS) cultured with 5 mM DCA compared to the untreated control using Neubauer chamber. (*D*) BrdU assay and (*E*) 3H-thymidine assay were conducted to analyze the proliferation rate of mesenchymal stromal cells (MSC; n=5). Neg Ctrl = Negative control cells treated with 1 µg/ml actinomycin D to suppress transcription and thus proliferation. Pos. Ctrl = 100% StemMACS™. Dichloroacetate (DCA) in different concentrations: 1, 5, 10, 25 mM. Statistical significance was determined using the Wilcoxon matched-pairs signed rank test. All data are shown as boxplots with median, interquartile range, max and min values and all data points; p-values are indicated in the graphs with *p<0.05, **p<0.01, ***p<0.001, ns=not significant.

Supplementary Tables

Supplementary Table 1. Donor information.

Synovial fibroblasts from OA patients			Mesenchymal stromal cells from OA patients			Synovial fibroblasts from trauma patients		
Donor	**Age**	**Sex**	**Donor**	**Age**	**Sex**	**Donor**	**Age**	**Sex**
FLS 1	58	m	MSC 1	62	w	non-OA 1	26	m
FLS 2	66	w	MSC 2	58	m	non-OA 2	25	w
FLS 3	81	w	MSC 3	52	m	non-OA 3	28	m
FLS 4	84	m	MSC 4	64	w	non-OA 4	29	w
FLS 5	83	m	MSC 5	65	m	non-OA 5	21	m
FLS 6	70	m	MSC 6	74	m			
FLS 7	67	m	MSC 7	71	m			
FLS 8	67	w	MSC 8	56	m			
FLS 9	71	w	MSC 9	48	w			
FLS 10	81	w	MSC 10	76	w			
FLS 11	70	w	MSC 11	86	m			
FLS 12	71	w	MSC 12	63	w			
FLS 13	66	m	MSC 13	74	w			
FLS 14	59	m	MSC 14	70	m			
FLS 15	80	w	MSC 15	56	w			
FLS 16	87	w	MSC 16	73	w			

Supplementary Table 4. List of GO-terms of synovial fibroblasts.

Category value	Total size	Selection size	Category size	Intersection size	Enrichment factor	P-value	Benj. Hoch. FDR
RNA metabolic process	6214	389	1179	22	0,29808	4,11E-15	1,20E-12
nucleobase-containing compound metabolic process	6214	389	1576	49	0,49666	7,78E-11	1,13E-08
small molecule metabolic process	6214	389	1226	123	1,6026	2,99E-09	2,90E-07
RNA processing	6214	389	490	6	0,1956	1,20E-08	8,76E-07
macromolecule metabolic process	6214	389	2660	117	0,70263	3,01E-08	1,75E-06
mRNA metabolic process	6214	389	442	6	0,21685	1,77E-07	8,58E-06
cellular nitrogen compound metabolic process	6214	389	1822	77	0,67509	2,99E-06	0,0001089
vitamin metabolic process	6214	389	70	16	3,6513	3,55E-06	0,00011479
alcohol metabolic process	6214	389	266	36	2,1619	4,47E-06	0,00012661
response to chemical stimulus	6214	389	1229	111	1,4428	4,79E-06	0,00012661
cellular ketone metabolic process	6214	389	434	50	1,8404	7,12E-06	0,0001727
organic acid metabolic process	6214	389	428	49	1,8288	1,03E-05	0,0002147
mRNA processing	6214	389	300	4	0,21299	1,83E-05	0,00035577
cellular lipid metabolic process	6214	389	356	42	1,8846	2,16E-05	0,00038347
lipid metabolic process	6214	389	445	49	1,759	2,78E-05	0,00044988
response to stimulus	6214	389	2373	184	1,2386	3,33E-05	0,00051029
hormone metabolic process	6214	389	51	12	3,7587	4,21E-05	0,00061256
biosynthetic process	6214	389	1547	68	0,70217	7,74E-05	0,000979
multicellular organismal process	6214	389	873	80	1,4639	7,24E-05	0,000979
nitrogen compound metabolic process	6214	389	1899	88	0,74025	7,49E-05	0,000979
protein targeting	6214	389	288	5	0,27733	0,00013761	0,0016018
cellular aldehyde metabolic process	6214	389	27	8	4,7331	0,00014652	0,0016399
viral reproduction	6214	389	427	11	0,41152	0,00016252	0,0017516
homeostatic process	6214	389	431	45	1,6678	0,00018354	0,0018624
xenobiotic metabolic process	6214	389	68	13	3,0539	0,0001856	0,0018624
protein transport	6214	389	734	26	0,56585	0,00019656	0,0019066
cellular aromatic compound metabolic process	6214	389	97	16	2,6349	0,00020849	0,0019515
cell activation	6214	389	222	27	1,9428	0,00034646	0,0029653
response to drug	6214	389	147	20	2,1734	0,00047597	0,0039573
organelle organization	6214	389	1254	56	0,71337	0,00056343	0,0045544
ion transport	6214	389	222	26	1,8709	0,00074023	0,0058218
multi-organism process	6214	389	247	28	1,8109	0,00078256	0,0059927
response to stress	6214	389	1136	92	1,2937	0,0011549	0,0086172
cellular component organization	6214	389	2206	114	0,82551	0,0012807	0,008967
developmental process	6214	389	1555	120	1,2327	0,0012511	0,008967
regulation of transport	6214	389	481	45	1,4945	0,0015213	0,010296
behavior	6214	389	129	17	2,1051	0,0016151	0,010681
biological regulation	6214	389	3438	239	1,1105	0,0017988	0,011632
carbohydrate metabolic process	6214	389	380	37	1,5554	0,0019021	0,012033
digestion	6214	389	5	3	9,5846	0,0021422	0,012467
heterocycle metabolic process	6214	389	266	28	1,6815	0,0021384	0,012467
response to endogenous stimulus	6214	389	422	40	1,5142	0,0020604	0,012467
amine metabolic process	6214	389	331	33	1,5926	0,0022007	0,012557
detection of stimulus	6214	389	70	11	2,5102	0,0026339	0,01474
response to biotic stimulus	6214	389	222	24	1,727	0,0029413	0,01585
extracellular matrix organization	6214	389	187	21	1,7939	0,0033086	0,0166
extracellular structure organization	6214	389	187	21	1,7939	0,0033086	0,0166
cellular ion homeostasis	6214	389	176	20	1,8153	0,0035486	0,017364
response to oxidative stress	6214	389	152	18	1,8917	0,0035801	0,017364
cellular homeostasis	6214	389	253	26	1,6416	0,0038528	0,01838

Supplementary Table 5. List of GO-terms of mesenchymal stromal cells.

	Category value	Total size	Selection size	Category size	Intersection size	Enrichment factor	P-value	Benj. Hoch. FDR
Mesenchymal stromal cells	extracellular matrix organization	6214	209	187	28	4,4519	1,20E-11	1,75E-09
	extracellular structure organization	6214	209	187	28	4,4519	1,20E-11	1,75E-09
	biological adhesion	6214	209	276	33	3,5549	7,88E-11	5,73E-09
	cell adhesion	6214	209	275	33	3,5678	7,15E-11	5,73E-09
	cellular amino acid metabolic process	6214	209	230	27	3,4903	7,05E-09	4,10E-07
	tRNA aminoacylation for protein translation	6214	209	43	12	8,2973	8,64E-09	4,19E-07
	amine metabolic process	6214	209	331	32	2,8744	3,01E-08	1,25E-06
	muscle contraction	6214	209	81	14	5,1389	3,26E-07	1,19E-05
	organic acid metabolic process	6214	209	428	34	2,3619	1,12E-06	3,62E-05
	cellular ketone metabolic process	6214	209	434	34	2,3292	1,52E-06	4,44E-05
	tRNA metabolic process	6214	209	88	13	4,3922	5,19E-06	0,00013724
	cell junction organization	6214	209	105	14	3,9643	7,55E-06	0,00018317
	multicellular organismal process	6214	209	873	52	1,771	8,69E-06	0,00019455
	locomotion	6214	209	431	30	2,0695	5,69E-05	0,0011823
	cellular component movement	6214	209	420	29	2,0529	8,61E-05	0,001671
	cellular metabolic process	6214	209	3385	89	0,78173	0,00012276	0,0022326
	cell motility	6214	209	276	21	2,2622	0,00022402	0,0036217
	cytoskeleton organization	6214	209	374	25	1,9874	0,00040339	0,0058693
	primary metabolic process	6214	209	3237	88	0,80829	0,00075078	0,010404
	organic acid transport	6214	209	49	7	4,2474	0,00094031	0,012047
	RNA processing	6214	209	490	6	0,36407	0,0013197	0,015361
	phosphorus metabolic process	6214	209	436	5	0,34096	0,001728	0,018624
	developmental process	6214	209	1555	69	1,3193	0,001866	0,018931
	homeostatic process	6214	209	431	5	0,34492	0,0019516	0,018931
	response to external stimulus	6214	209	472	27	1,7008	0,0021092	0,019799

Supplementary Table 6. Identification of mitochondrial proteins using mass spectrometry.

	Mitochondrial proteins	Mitochondrial proteins membrane	Mitochondrial proteins respiratory chain	Mitochondrial proteins ribosome
all	697	228	59	40
regulated FDR5%	121	40	5	2
regulated FDR1%	45	15	0	0
FLS FDR5%	99	36	4	2
FLS FDR1%	35	15	0	0
MSC FDR5%	22	4	1	0
MSC FDR1%	10	0	0	0